Nonlinear response of dense colloidal suspensions under oscillatory shear: Mode-coupling theory and Fourier transform rheology experiments

J. M. Brader,[1] M. Siebenbürger,[2] M. Ballauff,[2] K. Reinheimer,[3] M. Wilhelm,[3] S. J. Frey,[4] F. Weysser,[5] and M. Fuchs[5]
[1]*Department of Physics, University of Fribourg, CH-1700 Fribourg, Switzerland*
[2]*Helmholtz Zentrum für Materialien und Energie, D-14109 Berlin, Germany*
[3]*Karlsruhe Institute of Technology, D-76128 Karlsruhe, Germany*
[4]*Institut Charles Sadron, Université de Strasbourg, CNRS UPR 22, 23 rue du Loess, 67034 Strasbourg, France*
[5]*Fachbereich Physik, Universität Konstanz, D-78457 Konstanz, Germany*
(Received 12 October 2010; published 13 December 2010)

Using a combination of theory, experiment, and simulation we investigate the nonlinear response of dense colloidal suspensions to large amplitude oscillatory shear flow. The time-dependent stress response is calculated using a recently developed schematic mode-coupling-type theory describing colloidal suspensions under externally applied flow. For finite strain amplitudes the theory generates a nonlinear response, characterized by significant higher harmonic contributions. An important feature of the theory is the prediction of an ideal glass transition at sufficiently strong coupling, which is accompanied by the discontinuous appearance of a dynamic yield stress. For the oscillatory shear flow under consideration we find that the yield stress plays an important role in determining the nonlinearity of the time-dependent stress response. Our theoretical findings are strongly supported by both large amplitude oscillatory experiments (with Fourier transform rheology analysis) on suspensions of thermosensitive core-shell particles dispersed in water and Brownian dynamics simulations performed on a two-dimensional binary hard-disk mixture. In particular, theory predicts nontrivial values of the exponents governing the final decay of the storage and loss moduli as a function of strain amplitude which are in good agreement with both simulation and experiment. A consistent set of parameters in the presented schematic model achieves to jointly describe linear moduli, nonlinear flow curves, and large amplitude oscillatory spectroscopy.

DOI: 10.1103/PhysRevE.82.061401 PACS number(s): 82.70.Dd, 83.60.Df, 83.10.Gr

I. INTRODUCTION

A standard method to probe the viscoelastic character of a material is to measure the time-dependent stress response to an externally applied oscillatory shear field [1]. The simplicity of oscillatory shearing experiments presents distinct practical advantages when compared to other flow protocols and thus makes desirable a systematic method for the rheological characterization of a material on the basis of the periodic stress response alone. For small strain amplitudes the shear stress is a simple harmonic function, oscillating with the fundamental frequency dictated by the applied strain field. The details of the microscopic interactions underlying the macroscopic stress response are encoded in the familiar storage (G') and loss (G'') moduli of linear response. General aspects of the viscoelastic character of the material can thus be inferred from the magnitudes of the moduli as a function of frequency.

While, for many systems of interest, the linear-response regime is well understood, for practical applications, such as the production and processing of materials in industry [2], it is necessary to consider deformations of finite, often large, amplitude. In the nonlinear regime, the stress response to a sinusoidal excitation contains higher harmonic contributions, which arise from the nonlinearity of the underlying constitutive relation expressing the stress as a function of the strain [3–5]. For many complex materials, consideration of the fundamental frequency alone proves insufficient for describing the physical mechanisms at work for finite strain amplitude. Analysis based purely on the linear complex modulus as a function of frequency can thus be expected to give only a partial mechanical characterization of the system under study (see, e.g., [6–8]). This failing is found to be particularly pronounced for yield stress materials such as aqueous foams [9] and, as we will argue in the present work, colloidal suspensions close to or beyond the point of dynamical arrest. Although such systems are predominately elastic in character, they exhibit a complex transient response to oscillatory shear in which the viscous dissipation mechanism present at small strain amplitudes crosses over to a plastic flow as the amplitude is increased. The nonlinear stress response reflecting the onset of plastic flow gives rise to a strong increase in the amplitudes of the higher harmonics.

The emerging discipline of Fourier transform (FT) rheology, originating in the work of Wilhelm and co-workers (see, e.g., [4,5,10,11]), aims to quantify the nonlinear response of complex fluids by analyzing the harmonic structure of the stress signal measured in large amplitude oscillatory shear (LAOS) experiments (for recent developments see [12]). Despite considerable progress on the experimental side, the theoretical description of the nonlinear regime remains unsatisfactory. Theoretical treatments capable of capturing higher harmonic contributions have been largely restricted to phenomenological models based on the ideas of continuum rheology [3,8,10,13–15]. A more refined description of the nonlinear response is provided by mesoscopic models in which the time evolution of explicit coarse-grained degrees of freedom is governed by specified dynamical rules [16–18]. While such approaches are capable of capturing generic features of the response, they are not material specific and make

no explicit reference to the underlying particle interactions.

Recently, progress in making the connection between microscopic and macroscopic levels of description has been made for the case of dense colloidal suspensions subject to time-dependent flow [19,20]. The developments in classical nonequilibrium statistical mechanics presented in [19,20] extend earlier work focused on the simpler, but fundamental, case of steady shear flow [21,22]. The mode-coupling-type approximations employed in [19–22] capture the slow structural relaxation leading to dynamical arrest in strongly coupled systems (i.e., dispersions at high volume fraction or with a strongly attractive potential interaction), with the consequence that the macroscopic flow curves $\sigma(\dot{\gamma})$ attain a finite value in the limit of vanishing rate, for states which would be glasses or gels in the absence of flow. The finite value of the stress in the slow flow limit identifies the *dynamic* yield stress. The relationship between the dynamic yield stress and its more familiar static counterpart is analogous to that between stick and slip friction in engineering applications. A prediction of particular importance made by the mode-coupling theory (MCT)-based approaches in [19–22] is that the dynamic yield stress appears discontinuously as a function of coupling strength, in clear contrast to mesoscopic models [16,17] which predict a continuous power-law dependence. The notion of yield stress was considered in a more general and abstract sense in [23], in which a dynamic yield stress surface, describing yielding under more general nonshear deformations, was calculated (see also [24]).

Although the closed microscopic constitutive equation presented in [20] is of considerable generality, the combined difficulties of a large time-scale separation between microscopic and structural relaxation times, spatial anisotropy, and lack of time-translational invariance presented by many problems of interest make direct numerical solution of the equations impossible at the present time. In order to both facilitate numerical calculations and expose more transparently the essential physics captured by the fully microscopic theory in [20] a simplified "schematic" model has been proposed [23]. Schematic models have proved invaluable in the analysis and assessment of microscopic mode-coupling approaches, both for quiescent systems [25] and under steady shear flow [26], in each case providing a simpler set of equations which aim to retain the essential mathematical structure of the fully microscopic theory. While the schematic model reduction performed in [23] leads to loss of the "first-principles" character of the approach, the mathematical connections between full and schematic theories nevertheless serve to elevate the schematic model above purely phenomenological approaches.

In the present work we will consider application of the schematic model derived in [23] to the problem of large amplitude oscillatory shear. Although the tensorial schematic model in [23] is closely related to the earlier $F_{12}^{\dot{\gamma}}$ model derived in [26], application of the tensorial model to a simple shear flow geometry does not exactly reproduce the $F_{12}^{\dot{\gamma}}$ model. The study of time-dependent flows, not considered in earlier work, revealed that corrections to the original $F_{12}^{\dot{\gamma}}$ model were necessary to capture correctly the response to rapidly varying flows. The modifications thus introduced lead to small differences in the steady-state rheological predictions. Nevertheless, the present schematic models describe the same phenomenology as the previous model [27] when applied to steady shear.

Comparison of theoretical predictions with experimental data for thermosensitive core-shell particles, dispersed in water, has been performed using the $F_{12}^{\dot{\gamma}}$ model [26]. These particles have the very convenient feature that the volume fraction of the system may be varied continuously over a considerable range, simply by tuning the temperature of the system. Moreover, the finite polydispersity in particle size effectively suppresses crystallization, such that studies of dense fluid and glassy states are not complicated by an intervening fluid-crystal transition. In a series of works, theory and experiment have been compared for the flow curves under steady shear [28,29] and, more recently, for both flow curves and linear-response moduli [30,31]. A particular strength of the $F_{12}^{\dot{\gamma}}$ model (inherited by the more recent model of [23]) is that both flow curves and linear viscoelastic moduli can be simultaneously and accurately fitted over many decades of shear rate and frequency, respectively, using a consistent and physically meaningful set of fit parameters. In [31] a combination of experimental techniques was employed, which enabled measurement of the flow curves and linear-response moduli over eight and nine orders of magnitude in shear rate and frequency, respectively [31]. Although certain discrepancies between experiment and theory at low frequencies remain to be fully understood, the general level of agreement is impressive. Reassuringly for the schematic models, the complete microscopic MCT calculations possible for the linear-response moduli agree with the data from the monodisperse samples on the 40% error level [29].

The nonlinear rheology of thermosensitive microgel particles (similar to those considered in the present work) was addressed in a recent experimental study, focusing on the stress response to steady and large amplitude oscillatory flow [32]. In addition to the study of the stress overshoot following the onset of shear flow (see also [33]), both the strain dependence of the storage and loss moduli and the higher harmonic contributions were analyzed. Despite employing the same kind of thermosensitive particles and LAOS flow protocol, the study [32] should be regarded as complementary to the present work. In [32] volume fractions well above random close packing were investigated ($\phi > 0.64$), suggesting considerable deformation of the particles themselves, whereas we focus here on packing fractions around the glass transition. Moreover, emphasis in the present work is placed on assessing the MCT-based schematic theory presented in [23] for a nontrivial flow history, namely, large amplitude oscillatory shear, and comparison of the theoretical predictions with experiment. This comparison provides the first truly time-dependent test of this recently developed schematic model beyond the simple case of step strain already considered in [23].

The paper will be organized as follows. In Sec. II we summarize the microscopic starting points underlying our theoretical approach before proceeding to give a compact overview of the linear and nonlinear responses of viscoelastic systems, relevant for the subsequent analysis. In Sec. III we introduce the schematic MCT model and discuss its rela-

tion to previous work. In Sec. IV we discuss the Brownian dynamics simulation algorithm used to generate results supplementary to those of theory and experiment. Section V contains the experimental details. In Sec. VI we first present purely theoretical results in order to establish the phenomenology predicted by the schematic model. We then consider the results of our two-dimensional simulations before proceeding to analyze and fit the experimental data. Finally, in Sec. VII we discuss the significance of the present work and provide an outlook for future studies.

II. FUNDAMENTALS

A. Microscopic starting points

The shear stress resulting from a general time-dependent shear strain of rate $\dot{\gamma}(t)$ is given by a generalized Green-Kubo relation [19,20]

$$\sigma(t) = \int_{-\infty}^{t} dt' \dot{\gamma}(t') G(t,t'). \tag{1}$$

Equation (1) is nonlinear in the shear rate due to the nonlinear functional dependence of the shear modulus $G(t,t')$ on $\dot{\gamma}(t)$. Within the microscopic framework developed in [19,20] the modulus is identified as the correlation function of fluctuating stresses,

$$G(t,t') = \frac{1}{k_B T V} \left\langle \hat{\sigma}_{xy} \exp_{-}\left(\int_{t'}^{t} ds \Omega^{\dagger}(s) \right) \hat{\sigma}_{xy} \right\rangle, \tag{2}$$

where $\hat{\sigma}_{xy} \equiv -\Sigma_i F_i^x y_i$ is a fluctuating stress tensor element, formed by a weighted sum of the forces acting on the particles for a given configuration, T is the temperature, V is the system volume, and $\langle \cdot \rangle$ indicates an equilibrium average. The particle dynamics to be considered in the present work are generated by the adjoint Smoluchowski operator [34]

$$\Omega^{\dagger}(t) = \sum_i D_0 [\partial_i + \beta \mathbf{F}_i] \cdot \partial_i + D_0 \dot{\gamma}(t) y_i \frac{\partial}{\partial x}, \tag{3}$$

where $\beta = 1/k_B T$ and D_0 is the short-time diffusion coefficient at infinite dilution. The time-ordered exponential function in Eq. (2) arises because $\Omega^{\dagger}(t)$ does not commute with itself for different times [35].

An important approximation underlying Eq. (3) [and thus Eq. (2)] is that solvent induced hydrodynamic interactions (HIs) between the colloidal particles are neglected. The diffusion coefficient entering Eq. (3) is thus a scalar quantity and the external flow may be included using a prescribed (as opposed to self-consistently calculated) shear field $\dot{\gamma}(t)$. While the omission of HI may be inappropriate at high shear rates, for which hydrodynamically induced shear thickening can occur in certain systems, it is expected to represent a reasonable approximation for slowly sheared states close to the glass transition. Nevertheless, when attempting to fit experimental data using theoretical models based on Eq. (3) it proves necessary to include an empirical hydrodynamic correction accounting for the high-frequency viscosity. In addition to the neglect of HI we make two, potentially more dangerous, assumptions: (i) $\dot{\gamma}(t)$ is taken to be spatially translationally invariant, which may become questionable when considering the flow response of dynamically arrested states. (ii) The shear field acts instantaneously. While this should be acceptable for certain flow histories the general status of this approximation is not clear.

B. Linear response

Following standard convention, we consider an externally applied shear strain of the form

$$\gamma(t) = \gamma_0 \sin(\omega t). \tag{4}$$

The time-translational invariance of shear field (4) gives rise to an explicit dependence of modulus (2) upon two-time arguments.

For small deformation amplitudes ($\gamma_0 \ll 1$) the strain dependence of the shear modulus may be neglected, such that Eq. (1) provides a linear relationship between $\dot{\gamma}(t)$ and $\sigma(t)$. This leads to the approximation

$$G(t,t') = G_{\mathrm{eq}}(t-t'), \tag{5}$$

where $G_{\mathrm{eq}}(t)$ denotes the time-translationally invariant equilibrium shear modulus. Substituting Eqs. (4) and (5) into Eq. (1) and employing trigonometric addition formulas lead directly to the familiar linear-response result,

$$\sigma(t) = \gamma_0 G'(\omega)\sin(\omega t) + \gamma_0 G''(\omega)\cos(\omega t), \tag{6}$$

where $G'(\omega)$ and $G''(\omega)$ are the storage and loss moduli, respectively, defined by

$$G'(\omega) = \omega \int_0^{\infty} dt' \sin(\omega t') G_{\mathrm{eq}}(t'), \tag{7}$$

$$G''(\omega) = \omega \int_0^{\infty} dt' \cos(\omega t') G_{\mathrm{eq}}(t'). \tag{8}$$

Furthermore, Eq. (6) can be rewritten as

$$\sigma(t) = \gamma_0 |G(\omega)| \sin[\omega t + \delta(\omega)], \tag{9}$$

where the complex modulus is given by $G = G' + iG''$ and the phase shift by $\delta = \arctan(G''/G')$. If $G''(\omega) = 0$ the response is purely elastic, in phase with $\gamma(t)$ ($\delta = 0$). In the case $G'(\omega) = 0$ dissipation dominates and the response is in phase with $\dot{\gamma}(t)$ ($\delta = 90°$).

C. Nonlinear response

It should be clear at this stage that the familiar linear-response form (6) is a direct consequence of the convolution integral which results from inserting the time-translationally invariant equilibrium function (5) into Eq. (2). For finite strain amplitudes, the dependence of the modulus upon two-time arguments prevents the simple trigonometric manipulations leading to Eq. (6). Nevertheless, the nonsinusoidal stress response, $\sigma(t)$, is periodic with period $2\pi/\omega$ and may therefore be expressed as a Fourier series,

$$\sigma(t) = \gamma_0 \sum_{n=1}^{\infty} G_n'(\omega)\sin(n\omega t) + \gamma_0 \sum_{n=0}^{\infty} G_n''(\omega)\cos(n\omega t), \tag{10}$$

where G_n' and G_n'' are frequency dependent Fourier coefficients given by [36]

$$G_n'(\omega) = \frac{\omega}{\pi}\int_{-\pi/\omega}^{\pi/\omega} dt\sigma(t)\sin(n\omega t), \tag{11}$$

$$G_n''(\omega) = \frac{\omega}{\pi}\int_{-\pi/\omega}^{\pi/\omega} dt\sigma(t)\cos(n\omega t). \tag{12}$$

In the limit $\gamma_0 \to 0$ the coefficients G_1' and G_1'' reduce to the familiar linear-response moduli. It should be noted that we retain the $n=0$ term in the second sum of Eq. (10) in order to leave open the possibility of a stress offset.

Employing manipulations analogous to those leading from Eq. (6) to Eq. (9) Fourier series (10) may be expressed in the following form:

$$\sigma(t) = \gamma_0 \sum_{n=1}^{\infty} I_n(\omega)\sin[n\omega t + \delta_n(\omega)], \tag{13}$$

where the amplitude is given by $I_n = |G_n' + iG_n''|$ and the phase shifts by $\delta_n(\omega) = \arctan(G_n''/G_n')$. In analyzing our theoretical, experimental, and simulation results we will focus on the behavior of both the generalized moduli G_n' and G_n'' and the amplitude and phase shift, I_n and δ_n, of the fundamental ($n=1$) and higher harmonics ($n>1$) as a function of the control parameters.

Following a period of transient response after initiation of the strain field (switching on the rheometer) the system enters a stationary state, demonstrating a periodic stress response. Although, to some extent, an issue of semantics, it is important that the "stationary" state presently under consideration be distinguished from "steady" states, of the kind achievable by application of a time-independent shear flow. The stationary state is simply a well-characterized and periodic transient and is thus influenced by additional physical mechanisms (e.g., thixotropy) which are irrelevant for steady states. In a physical system the stationary response must be independent of the direction of shear, leading to a stress $\sigma(t)$ symmetric in $\dot{\gamma}(t)$. The mirror symmetry of the constitutive equation has the consequence that only odd terms contribute to Fourier series (13). The appearance of even harmonics in the analysis of experimental data is often an indication of boundary effects, such as wall slip, or other inhomogeneities of the flow [10].

Important physical interpretation may be given to the coefficient G_1'' by considering the energy dissipated per unit volume of material per oscillation cycle,

$$E_d = \int_{-\pi/\omega}^{\pi/\omega} dt\sigma(t)\dot{\gamma}(t). \tag{14}$$

Substitution of strain field (4) and Fourier series (10) into Eq. (14) leads to

$$E_d = \gamma_0^2 \pi G_1''(\omega) \tag{15}$$

(see also [37]). Thus, for a sinusoidal strain of form (4), energy is dissipated only at the input frequency. The coefficient G_1'' therefore has the same interpretation in the nonlinear regime as in the linear regime: it determines the dissipation of energy over an oscillation cycle. The remaining coefficients in the series, G_n' and $G_{n>1}''$, thus collectively describe the reversible storage and recovery of elastic energy.

D. Lissajous plots

A standard way to graphically represent the relationship between $\gamma(t)$ and $\sigma(t)$ is via the Lissajous representation, in which trajectories are shown in the γ^*, σ^* plane, where $\gamma^* = \gamma/\gamma_{\max}$ and $\sigma^* = \sigma/\sigma_{\max}$ are the strain and stress, normalized by their maximum values [38]. In this representation, a general *linear* viscoelastic response is characterized by an ellipse symmetric about the line $\gamma^* = \sigma^*$, point symmetric with respect to the origin plus two mirror planes. The two limiting cases of a purely elastic and a purely dissipative response are thus characterized by a line and a circle, respectively. In the nonlinear regime considerable deviations from ellipticity are observed. The specific character of these deviations can indicate whether a material is, for example, strain hardening or strain softening (an increase or decrease of G' with strain amplitude) and thus provides a useful, albeit qualitative, "rheological fingerprint" of a given material [6,8]. For a general nonlinear response, the area enclosed within the closed-loop trajectory of a Lissajous figure is directly related to the dissipated energy via the integral in Eq. (14). This lends an appealing physical interpretation to the Lissajous representation and provides a direct visual impression of the dissipative character of the response.

III. THEORETICAL APPROACH

A. Schematic model

As noted in Sec. I, the approximate microscopic constitutive theory developed in [19,20] enables first-principles prediction of the rheological behavior of dense colloidal dispersions. However, the simultaneous occurrence of spatial anisotropy and non-time-translational invariance hinders numerical solution of the equations when addressing concrete problems. The schematic model presented in [23] provides a simplified set of equations which, it is hoped, capture the essential physics contained within the full equations while remaining tractable for numerical implementation.

Within the schematic reduction, the modulus is expressed in terms of a single-mode transient density correlator

$$G(t,t') = v_\sigma \Phi^2(t,t'), \tag{16}$$

where v_σ is a parameter measuring the strength of stress fluctuations. The approximation underlying Eq. (16) is that stress fluctuations relax as a result of relaxations in the density (viz., structural relaxation). The assumption that v_σ is independent of strain is a simplifying assumption which could be relaxed if necessary. The microscopic theory in [20] predicts both the temporal and wave-vector dependences of

the transient density correlator under applied flow. The schematic, single-mode, density correlator [normalized to $\Phi(t,t)=1$] represents, in some nonspecific sense, a "typical" correlator of the microscopic theory. It is obtained from solution of a nonlinear integrodifferential equation,

$$\dot{\Phi}(t,t') + \Gamma\left(\Phi(t,t') + \int_{t'}^{t} ds m(t,s,t')\dot{\Phi}(s,t')\right) = 0. \quad (17)$$

The single decay rate Γ sets the time scale and would, within a microscopically based theory, depend on both structural and hydrodynamic correlations. The overdots in Eq. (17) imply differentiation with respect to the first time argument. The memory function $m(t,s,t')$ appears in Eq. (17) as a generalized friction kernel, which can be formally identified as the correlation function of certain stress fluctuations. Making the assumption that these stress fluctuations may be expressed in terms of density fluctuations (both become slow close to the glass transition) leads to a tractable expression for $m(t,s,t')$ as a quadratic functional of the transient density correlator and, thus, a closed theory. A somewhat surprising consequence of the formal calculations presented in [19,20] is that the memory function possesses three time arguments. The presence of a third time argument, which would have been difficult to anticipate on the basis of quiescent MCT intuition, has important consequences for rapidly varying flows (e.g., step strain [19]). Within the schematic model the memory function is given by

$$m(t,s,t') = h(t,t')h(t,s)[\nu_1\Phi(t,s) + \nu_2\Phi^2(t,s)]. \quad (18)$$

Following conventional MCT practice the parameters ν_1 and ν_2 represent, in an unspecified way, the role of the static structure factor in the microscopic theory and are chosen as $\upsilon_2=2$ and $\upsilon_1=2(\sqrt{2}-1)+\epsilon/(\sqrt{2}-1)$. The separation parameter ϵ is a crucial parameter within our approach and encodes the thermodynamic state point of the system by measuring the distance from the glass transition. Negative values of ϵ correspond to fluid states and positive values to glass states. Setting h equal to unity in Eq. (18) recovers the well-known F_{12} model, originally introduced by Götze [25,39,40]. The linear term in Φ which appears in Eq. (18) is absent from the microscopic mode-coupling expression but turns out to be necessary for a faithful reproduction of its asymptotic properties within a single-mode theory. Under simple shear flow, the h functions in the memory kernel (18) serve to accelerate the loss of memory caused by the affine advection of density fluctuations. The assumption that the same function h may be used to incorporate both the strain accumulated between t and t' as well as that between t and s is an approximation, made to keep the theory as simple as possible. Taking account of the required invariance with respect to flow direction suggests the simple ansatz,

$$h(t,t') = \frac{\gamma_c^2}{\gamma_c^2+\gamma^2}, \quad (19)$$

where $\gamma \equiv \gamma(t,t') = \int_{t'}^{t} ds\,\dot{\gamma}(s)$ and the parameter γ_c sets the scale of strain.

Equations (1) and (16)–(19) provide a closed constitutive theory which depends upon three adjustable parameters $(\upsilon_\sigma, \Gamma, \gamma_c)$ and two control parameters $(\epsilon, \dot{\gamma})$ representing the coupling strength and applied shear rate. As the schematic model under discussion is implicitly based on the Smoluchowski dynamics described by Eq. (3), the influence of HI is neglected. While this is not important for capturing correctly the qualitative features of the rheological response, quantitative comparison requires a simple hydrodynamic correction at high frequencies. The simplest approximation, which we will employ in the present work, is to empirically add an extra term to the shear modulus,

$$G(t,t') \to G(t,t') + \eta_\infty \delta(t-t'). \quad (20)$$

The high-frequency viscosity, η_∞, is thus introduced into the model, describing the viscous processes which occur on time scales much shorter than the structural relaxation time. Correction (20) has the consequence that the stress acquires an extra term, linear in $\dot{\gamma}$, and the Fourier coefficient G_1'' is shifted by a term linear in ω.

B. Strain-rate frequency superposition

An alternative mode-coupling-type approach, describing the collective density fluctuations of dense colloidal fluids under shear, is provided by the work of Miyazaki *et al.* [41–43]. By considering time-dependent fluctuations about the steady state a closed (scalar) constitutive equation has been derived and applied to colloidal dispersions in two dimensions under steady shear [41,42] and in three dimensions (subject to additional isotropic approximations) under large amplitude oscillatory shear [43]. Given the very different nature of the approximations underlying the present MCT-based theory [19–22] and that in [41–43] (fluctuating hydrodynamics vs projection operator methods) it is interesting that the final expressions (e.g., the memory function vertices entering the equation of motion for the transient correlator) are rather similar, at least for the special case of steady shear. For the case of large amplitude oscillatory shear, however, the theory presented in [43] differs clearly and fundamentally from the microscopic approaches to time-dependent shear developed in [19,20] and, consequently, from the schematic model in [23] to be employed in the present work. The theoretical developments of Miyazaki *et al.* [43] motivated the authors to propose the principle of "strain-rate frequency superposition" as a probe of structural relaxation in soft materials [44].

The essence of the approach of Miyazaki *et al.* can be captured by a simple schematic model, which we will elaborate upon below. In [43] Miyazaki *et al.* took the theory which they had developed for steady shear flow [41,42] and replaced the steady shear rate $\dot{\gamma}$ appearing in the equation of motion for the correlator by the time-dependent shear rate $\dot{\gamma}(t)=\gamma_0\omega\cos(\omega t)$, describing oscillatory flow. This rather *ad hoc* treatment gives rise to equations with a mathematical structure appropriate for steady flows and ignores the more realistic, although more complicated, history dependence of theories developed to treat nonsteady flows specifically [19,20]. On the basis of the results obtained for the strain amplitude dependence of the storage and loss moduli (notated as G_1', G_1'' in the present work) it was argued that the

time dependence of the strain-rate field $\dot{\gamma}(t)=\gamma_0\omega\cos(\omega t)$ is not essential for understanding the viscoelastic response and that it is sufficient to consider the strain-rate amplitude $\gamma_0\omega$ alone. The relevant time scale is thus identified as $(\gamma_0\omega)^{-1}$ rather than ω^{-1}. Within the context of schematic mode-coupling equations, this assumption may be expressed by the following memory function:

$$m(t)=\frac{[\nu_1\Phi(t)+\nu_2\Phi^2(t)]}{1+(\gamma_0\omega t)^2}, \tag{21}$$

which, together with the equation of motion

$$\dot{\Phi}(t)+\Gamma\left(\Phi(t)+\int_0^t dt' m(t-t')\dot{\Phi}(t')\right)=0, \tag{22}$$

the shear modulus

$$G(t,t')=v_\sigma\Phi^2(t-t'), \tag{23}$$

and Eq. (1) provides a closed theory for $\sigma(t)$. In fact, Eqs. (21)–(23) are identical to the $F_{12}^{\dot{\gamma}}$ model [25,26], with a steady shear rate $\dot{\gamma}=\gamma_0\omega$. An important consequence of assuming the dominance of the time scale $(\gamma_0\omega)^{-1}$ is that all states, even those which would be glasses in the absence of flow, become fluidized by an applied oscillatory shear field, regardless of the amplitude γ_0. Whether or not a vanishingly small value of γ_0 is really sufficient to restore ergodicity to dynamically arrested states is unclear and presents a fundamental question, with important implications for the existence of a linear-response regime.

Despite capturing approximately the amplitude dependence of G_1', G_1'', describing the response at the fundamental frequency, higher harmonics are ignored in the approach in [43]. The absence of higher harmonic contributions within the theory of Miyazaki *et al.* can be traced back to the assumption that the time dependence of $\dot{\gamma}(t)$ is irrelevant and that this can be represented by the constant $\gamma_0\omega$. Within the present context this has the consequence that memory function (21) and correlator, given by solution of Eq. (22), are constrained to be time-translationally invariant (viz., depend on a single correlation time only). While this assumption is clearly at odds with the underlying variations in the strain field (for which a dependence on the "waiting time" is to be expected), it nevertheless serves to capture first-order corrections to linear-response theory while remaining relatively easy to implement numerically.

The theory developed in [43] is quasilinear in the sense that $\sigma(t)$ remains a simple sinusoid but with an amplitude and phase shift which depend nonlinearly on γ_0. Attempts to justify the neglect of higher harmonics have been based on the fact that the ratio of the third harmonic amplitude to that of the fundamental remains smaller than approximately 20% for a wide range of systems [43,44]. However, in order to draw a fair conclusion, it is important to consider the sum $\Sigma_{n>1} I_n(\omega)/I_1$ rather than I_3/I_1 alone when assessing the physical relevance of higher harmonic contributions. Various experimental studies on colloidal dispersions (see, e.g., [32]) show clearly that the higher harmonics can collectively account for up to half of the total signal, which is not a small effect. This observation serves to emphasize the importance of truly nonlinear theories, which confront directly the non-time-translational invariance of the correlation functions, thus going beyond the convolution approximation to Eq. (1).

IV. COMPUTER SIMULATION

To provide a point of reference for our theoretical calculations we have performed two-dimensional simulations on a system hard disks undergoing Brownian motion in an external shear field. The simulations are designed to solve approximately the many-body problem of a system of interacting Brownian particles under shear flow. The same Smoluchowski dynamics [34] underlies the microscopic mode-coupling theories in [19,20] which form the basis of the schematic model employed in the present work [23]. We choose to simulate a two-dimensional system for two reasons: (i) The computational resources required are significantly reduced with respect to simulation of three-dimensional systems and thus enable improved statistics to be obtained. (ii) Recent microscopic studies of the quiescent mode-coupling theory in two dimensions have revealed behavior broadly similar to that found in three-dimensional calculations [45]. We thus expect the reduced dimensionality of our simulation system to be of little consequence for qualitative comparison with the present theory and experimental data.

The basic concept of the algorithm has been described in detail in three dimensions in [46] and its adaptation to two dimensions can be found in [47]. We consider a binary mixture of hard disks with the diameters of $D_s=1.0$ and $D_b=1.4$ with equal particle number concentrations and a total amount of $N=N_s+N_b=1000$ hard disks in a two-dimensional simulation box of volume V with periodic Lees Edwards boundary conditions. The total two-dimensional volume fraction is then given by $\phi_{\mathrm{tot}}=\frac{N\pi}{4V}(D_b^2+D_s^2)$. We employ this system in order to suppress crystallization effects. The mass m of the particles and k_BT are set equal to unity. We choose our coordinate axes such that flow is in the x direction and the shear gradient is in the y direction. The Brownian time step was chosen to be $\delta t=0.01$ as in [47]. This results in a short-time diffusion constant of $D_0=0.05$. To implement a time-dependent oscillatory shear rate, at each Brownian time step the shear rate is set to its new value,

$$\dot{\gamma}(\tau_B)=\gamma_0\omega\cos(\omega\tau_B), \tag{24}$$

and all particle velocities are freshly drawn from the Gaussian distribution with $\langle \boldsymbol{v}^2\rangle=2$ and $\langle \boldsymbol{v}\rangle=\dot{\gamma}(\tau_B)y(\tau_B)$. Between two Brownian time steps the shear rate is kept constant. The strain $\gamma(t)$ can, therefore, be obtained using

$$\gamma(t)=\sum_{\tau_B\in[0,t]}\dot{\gamma}(t_B)\delta t, \tag{25}$$

which leads to $\gamma(t)=\int_0^t dt\,\dot{\gamma}(t)$ in the limit of $\delta t\to 0$. At every Brownian time step the part $\dot{\gamma}(\tau_B)y(\tau_B)$ guarantees a linear velocity profile as a linear shear flow is imposed on every particle, depending on its y position. For all simulations the frequency was set to $\omega=0.001$ which leads to $\mathrm{Pe}_\omega\equiv\omega D^2/4D_0=0.05$.

The average quantity of interest in the present work is the time-dependent potential part of the shear stress $\sigma_{xy}(t) = \frac{1}{V}\langle\Sigma[\boldsymbol{F}(t)_{ij}]_x[\boldsymbol{r}(t)_{ij}]_y\rangle$, with the relative force components of particle i and j $[\boldsymbol{F}(t)_{ij}]_x$ and the particles relative distance component $[\boldsymbol{r}(t)_{ij}]_y$ for a given time t. As we consider hard particles the forces must be calculated from the collision events. By observing the collisions within a certain time window $\Delta\tau_c=[t_k,t_k+\Delta\tau_c]$ for a given time t_k, forces may be extracted using the change of momentum which occurs during the observation time. This leads to the evaluation algorithm for the stress at time t_k,

$$\sigma(t_k) = \left\langle \frac{1}{\Delta\tau_c} \sum_{t_c \in [t_k, t_k+\Delta\tau_c]} [\Delta\boldsymbol{v}(t_c)_{ij}]_x [\boldsymbol{r}(t_c)_{ij}]_y \right\rangle_s ,$$

where summation is over all collisions after time t_c within the time window $\Delta\tau_c$. The procedure effectively sums the momentum changes $(\Delta\boldsymbol{v}_{ij})_x$ in x direction multiplied by the relative distance of the particles $(\boldsymbol{r}_{ij})_y$ in y direction. The brackets $\langle\cdots\rangle_s$ denote the different simulation runs.

At a total volume fraction of $\phi_{\mathrm{tot}}=0.81$ which is slightly above the glass transition for this system (estimated to be at $\varphi=0.79$ on the basis of simulated flow curves [47]) we prepared 4000 independent sets for each amplitude $\gamma_0 \in \{0.001, 0.003, 0.009, 0.01, \ldots, 0.09, 0.1, 0.2, 1.0, 10.0, 100.0\}$. As the system starts from a nonstationary state it is necessary to wait for the system to reach its long-time asymptote (which we found to be the case after undergoing two full oscillations) before meaningful averages can be taken.

V. EXPERIMENT

A. Characterization of the latex particles

The polydisperse latex particles consist of a solid core of poly(styrene) onto which a thermosensitive network of cross-linked poly(*N*-isopropylacrylamide) is affixed [31]. The degree of cross-linking of the shell due to the cross-linker *N*,*N*′-methylenebisacrylamide is 2.5 mol %. Exactly the same particles were used for this work as in [31]. They have a temperature dependent size (hydrodynamic radius in nanometer, $R_H=-0.7796T+102.4096$, with T as the temperature in °C below 25 °C) and a polydispersity of 17% [31]. All experiments were done in an aqueous solution of 0.05*M* KCl to screen residual charges which emerge from the synthesis of the particles. The solid content of the suspension was determined by comparing the weight before and after drying and was found to be 8.35 wt %. Neither the MCR 301 measurements nor the FT-rheology measurements at 15.1 °C lead to a significant change of the solid content (+0.02 wt %). However, the solid content after the FT-rheology measurements at the remaining two temperatures (18.4 and 20.9 °C) had a slightly higher value (9.02 wt %) due to the physical relocation of the rheometer to another laboratory and some additional solvent evaporation. The effective volume fraction ϕ_{eff} was calculated by using the correlation of mass concentration c, hydrodynamic radius, and effective volume fraction found in the inset of Fig. 6 in [31], which is given by $c\cdot R_H^3=9.67\times10^{-17}g\cdot\phi_{\mathrm{eff}}$ for different temperatures. For the temperature of 15.0 °C a volume fraction ϕ_{eff} of 0.65, for 18.0 °C a ϕ_{eff} of 0.60, and for 20.0 °C a ϕ_{eff} of 0.57 were found. In previous work [31] the glass transition for this system was found to be at $\phi_{\mathrm{eff}}=0.64$. Given a polydispersity of 17% the theory of Schärtl and Sillescu [48] predicts random close packing at $\phi_{\mathrm{eff}}=0.68$.

B. Rheological experiments

1. Measurements with the MCR 301

The rheological experiments measured with the stress-controlled MCR 301 from Anton Paar with a Cone Plate geometry (diameter of 50 mm and cone angle of 0.017 rad) cover the range from the linear to the strongly nonlinear regime. This machine was used to measure the frequency dependent linear moduli, the shear-rate dependent flow curves, and the strain amplitude dependent nonlinear moduli. A thin paraffin layer was used to prevent the solution to evaporate. Measurements controlled by the Peltier heating were performed at 15.0, 18.0, and 20.0 °C with a preshear protocol of $\dot{\gamma}=100\ \mathrm{s}^{-1}$ lasting 200 s and a waiting time of 10 s before each experiment. The flow curves shown in Fig. 13 were measured with the MCR 301. Flow curves were measured from low to high shear rates (10^{-4}–1000 s^{-1}) and a waiting time of 10 s with a logarithmic time ramp of 20–2500 s. For the flow curve at 15.0 °C a larger measurement range was chosen: $\dot{\gamma}=10^{-4}$–10^3 with a logarithmic ramp of 20–10^4 s. The frequency tests were performed at a deformation of 1% starting from 10 to 0.001 Hz with a time ramp of 20 to 1000 s. The oscillatory deformation tests at 1, 0.1, and 0.01 Hz were performed with a measurement time of 100 s for each point. In all cases this assured that transients had decayed.

2. FT-rheological measurements with the ARES rheometer

For the FT-rheological measurements an ARES rheometer (Rheometrics Scientific) with a cone plate geometry (diameter of 50 mm and cone angle of 0.04 rad) was used. The ARES rheometer is a strain-controlled rheometer equipped with a dual range force rebalance transducer (which can measure a maximum torque of 0.01 Nm), capable of measuring torques ranging from 0.004 to 10 mN m, specified by the manufacturer. It has a high-resolution motor, applying frequencies from 10^{-5} to 500 rad s^{-1} and deformation amplitudes ranging from 0.005 to 500 mrad. A water bath adjusts the temperature. The FT-rheological setup consists of the ARES and a computer which either controls the rheometer via a serial cable as well as it detects the strain and torque outputs via BNC cables. The analog raw data of the measurements are digitized with a 16-bit analog-to-digital converter (ADC). This ADC card has a maximum sampling rate of 50 kHz per channel. Due to the high sampling rate the time between consecutive data points is very small compared to the time scale of rheological experiments. The loss of information by sampling the torque transducer data is negligible [52]. To achieve best results with respect to the signal-to-noise ratio, oversampling is applied. The ADC card acquires the time data at the highest possible sampling rate and then preaverages them on the fly to reduce random noise.

With this method the noise is reduced by a factor of 3–5 which could only be achieved by averaging multiple measurements [53]. Within the setup a 16-bit ADC card is implemented, which is able to discriminate steps. The quantification resolution of the ADC card limits the ratio. It determines the minimum detectable intensity of weak signals by its ability to discriminate the intensity of the signal. The higher the bit number, the smaller the detectable intensity variation [54]. After acquisition and digitization of the time data, they are handled with MATLAB software [50,51].

A solvent trap, equipped with a sponge drawn with water and an additional thin paraffin layer, is used to prevent evaporation. Frequency tests were used to compare the rheological results of the MCR 301 and the ARES rheometer. The temperature of the ARES was then adjusted to fit the results of the frequency tests of the MCR 301. Therefore, the FT-rheological measurements were performed at 15.1, 18.4, and 20.9 °C with the ARES rheometer (the high-temperature difference results from a change of location of the ARES after the measurements at 15.1 °C leading to a higher evaporation). After a preshear of $\dot{\gamma}=100\ s^{-1}$ lasting 200 s and a waiting time of 10 s, oscillatory time sweep measurements were started. The FT signal was always recorded after some oscillations, so that the suspension reached the oscillatory stationary state. Measurements were performed at frequencies of 1, 0.1, and 0.01 Hz at different deformation amplitudes. Typically for the nonlinear FT-rheology measurements with the time sweep tests 40 oscillations for 1 Hz excitation were applied, whereas 10 oscillations for 0.1 Hz and 9 oscillations for 0.01 Hz. To obtain a FT spectrum from the raw time data we performed a discrete, complex, half-sided fast Fourier transformation [5,11,49]. For further information of the setup, the measuring principal and FT analysis, we would like to refer to [50,51].

VI. RESULTS

A. Theoretical predictions

1. Flow curves

For given values of the parameters $(v_\sigma, \gamma_c, \Gamma, \epsilon)$ the schematic theory defined by Eqs. (1) and (16)–(19) enables prediction of the flow curve expressing the steady shear stress σ as a function of shear rate $\dot{\gamma}$. Figure 1 shows a set of typical flow curves generated by the schematic MCT model for three fluid states ($\epsilon<0$), the critical state ($\epsilon=0$), and three states in the glass ($\epsilon>0$). The parameters employed for the theoretical calculations presented in Fig. 1 (as well as for Figs. 2–7) are $v_\sigma=100$, $\gamma_c=0.15$, $\Gamma=100$, and $\epsilon=10^{-3}$. Experience with fitting the experimental data, to be considered in Sec. VI C, shows that these choices represent sensible physical values for the model parameters. In the fluid, there exists a linear (Newtonian) regime for small shear rates ($\mathrm{Pe}_0\equiv\dot{\gamma}/\Gamma\ll 1$), for which the standard F_{12} model result for the shear viscosity holds, $\sigma=\dot{\gamma}\int_0^\infty dt\Phi_{\mathrm{eq}}^2(t)\equiv\dot{\gamma}\eta$. Increasing the separation parameter to less negative values (corresponding to, e.g., an increase in the volume fraction) gives rise to an increase in η, reflecting the slowing of the structural relaxation time τ, which dominates all transport properties within our MCT approach. For $\dot{\gamma}\tau>1$ the effect of shear starts to dominate the structural relaxation and the stress increases sublinearly as a function of shear rate, corresponding to shear thinning of the viscosity $\eta(\dot{\gamma})=\sigma(\dot{\gamma})/\dot{\gamma}$. At high shear rates $\dot{\gamma}\tau\gg 1$ the present model yields $\sigma=\dot{\gamma}/\Gamma$ and needs to be supplemented by corrections which account for the high shear limiting viscosity (and which, in the absence of HI, are determined by the solvent contribution η_∞).

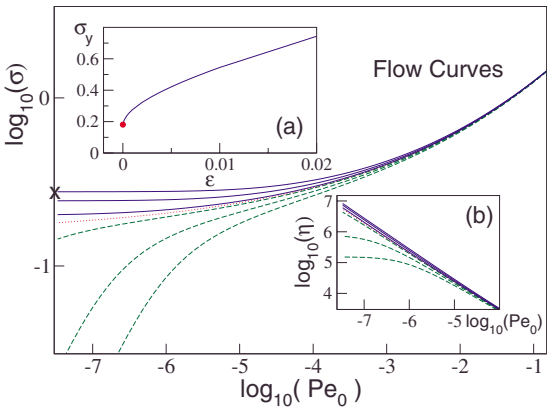

FIG. 1. (Color online) (Theory) The flow curves for fluid states $\epsilon=-10^{-3}$, -5×10^{-4}, -10^{-4} (green, dashed lines) at the critical point $\epsilon=0$ (red, dotted line) and for glassy states $\epsilon=10^{-4}$, 5×10^{-4}, 10^{-3} (blue, full lines). In the glass ($\epsilon>0$) there exists a finite stress in the limit of vanishing shear rate, identified with the dynamical yield stress ($\lim_{\dot{\gamma}\to0}=\sigma_y$). The cross indicates the yield stress value used in Figs. 3 and 4. Inset (a) shows the discontinuous emergence of a dynamical yield stress as a function of ϵ. Inset (b) shows the viscosity $\eta=\sigma/\dot{\gamma}$. Calculations were performed with $\eta_\infty=0$.

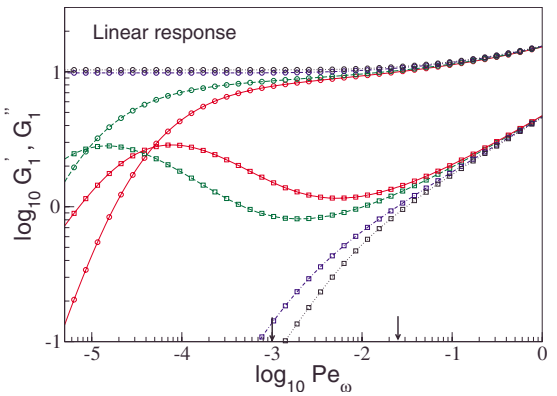

FIG. 2. (Color online) (Theory) The linear-response moduli G_1' (lines with circles) and G_1'' (lines with squares) as a function of Pe_ω for two state points in the fluid $\epsilon=-0.001$ (red, full line), -0.0005 (green, broken line), and two in the glass $\epsilon=0.0005$ (blue, dotted-dashed line) and 0.001 (black, dotted line). For fluid states the finite value of the structural relaxation-time scale is reflected in the maximum in G'' and the consequent crossing of G' and G'' at low frequency. The results presented here omit solvent hydrodynamics which may become relevant at $\mathrm{Pe}_\omega\approx1$ (calculations were performed with $\eta_\infty=0$). These will be included in a simple approximate fashion when fitting the experimental data. The two arrows indicate the values $\mathrm{Pe}_\omega=0.001$ and 0.025 used to generate Figs. 3 and 4, respectively.

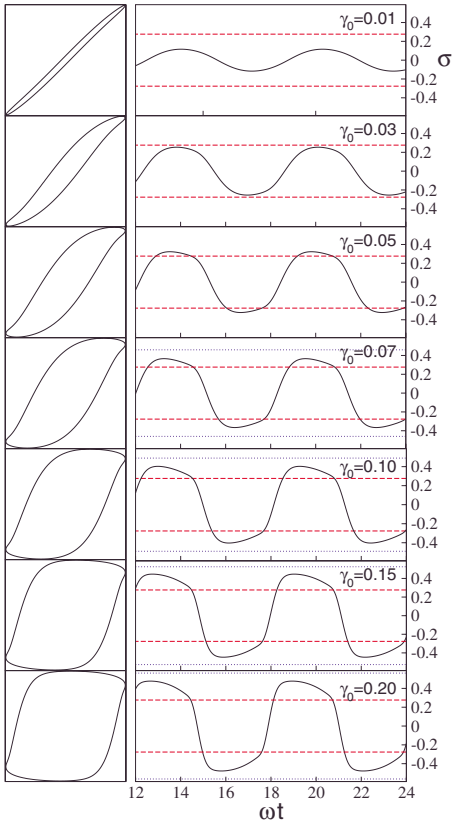

FIG. 3. (Color online) (Theory) The stress response of a glassy state to oscillatory strain calculated from our MCT-based theory for strain amplitudes from γ_0=0.01, 0.03, 0.05, 0.07, 0.10, 0.15, and 0.20. The associated Lissajous figures illustrate the nonlinear character of the response. The increase in dissipation with increasing γ_0 is reflected by the increasing area enclosed by the Lissajous curves. All calculations were performed at Pe_ω=0.025 and ϵ=0.001. The red horizontal broken lines indicate the dynamic yield stress obtained from the flow curve in Fig. 1 for ϵ=0.001 (σ_y=0.2763). The response becomes clearly nonlinear when the maximum of $\sigma(t)$ approaches the dynamical yield stress. The blue horizontal dotted lines provide an upper bound for the maximum of the time-dependent stress and are taken from the corresponding flow curve in Fig. 1.

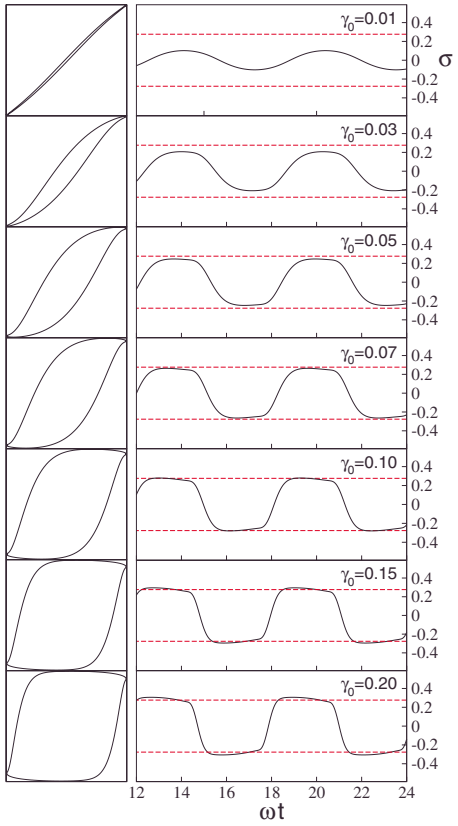

FIG. 4. (Color online) (Theory) As in Fig. 2 (ϵ=0.001) but for a lower frequency Pe_ω=0.001. At this value of Pe_ω the system is almost perfectly elastic in the linear regime ($G' \gg G''$ for $\gamma_0 \ll 1$; see Fig. 4). As the time-dependent stress exceeds the dynamical yield stress the signal becomes clipped. At this frequency $\sigma_{\max}$ lies very close to σ_y and has thus been omitted for clarity.

As $\epsilon \to 0^-$ the regime of linear response shifts to increasingly lower values of the shear rate and disappears entirely at the (ideal) glass transition, ϵ=0. For states in the glass there exists a finite stress in the limit of vanishing shear rate, identified as the dynamical yield stress $[\lim_{\dot\gamma \to 0} \sigma(\dot\gamma) = \sigma_y]$. Within idealized MCT-based treatments the dynamical yield stress emerges discontinuously as ϵ is varied across the glass transition (shown in the inset of Fig. 1). It should be mentioned that the flow curves shown in Fig. 1 differ quantitatively from those of the extensively studied $F_{12}^{\dot\gamma}$ model [26] due to the inclusion of an additional prefactor $h(t,t')$ in the expression for memory function (18). Nevertheless, the qualitative predictions of the theory for the flow curves are in full agreement with those of the $F_{12}^{\dot\gamma}$ model.

2. Linear response moduli

The linear storage and loss moduli, given by Eqs. (7) and (8), respectively, are shown in Fig. 2 as a function of $\mathrm{Pe}_\omega \equiv \omega/\Gamma$ for two fluid states (ϵ<0) and two glassy states (ϵ>0). In the fluid, the finite value of the structural relaxation-time scale τ is reflected in the maximum of G'' and the crossing of G' and G'' at low frequency. The fact that

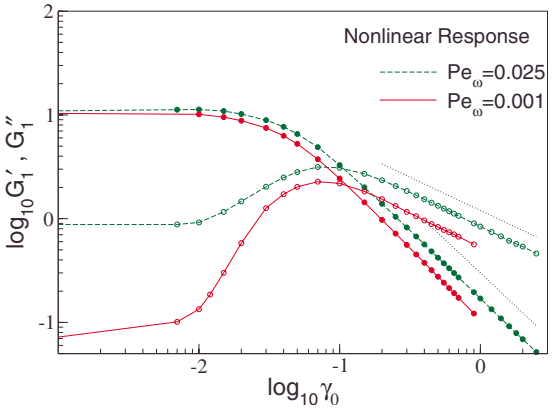

FIG. 5. (Color online) (Theory) The theoretical G_1' and G_1'' as a function of strain for ϵ=0.001 at frequencies Pe_ω=0.025 and Pe_ω=0.001. Points are the numerically calculated data points; lines are guide for the eyes. For large values of the strain the numerical data are well fitted by the power laws $G'' \sim \gamma_0^{-\nu}$ and $G' \sim \gamma_0^{-2\nu}$ with ν=0.65 (indicated by dotted lines).

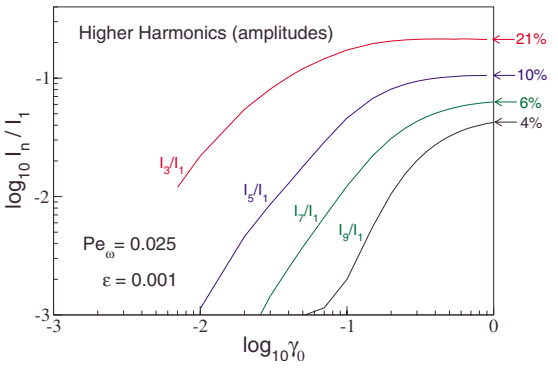

FIG. 6. (Color online) (Theory) The theoretical intensities of the third, fifth, seventh, and ninth harmonics which contribute to the nonlinear stress response shown in Fig. 2. At strains approaching unity the collective contribution of the higher harmonics accounts for approximately 50% of the total $\sigma(t)$ signal ($\epsilon=10^{-3}$ and $\mathrm{Pe}_\omega=0.025$).

G' remains notably larger than G'' at high frequencies is simply a result of neglecting the high-frequency limiting viscosity η_∞ in presenting our theoretical predictions. Setting $\eta_\infty=0$ in presenting the theory highlights the contribution of structural processes to the viscoelasticity. In the glass, G'' goes to zero at low frequencies ($G''\sim\omega$) and G' attains a finite low-frequency value, identifying the transverse elastic constant G_∞. Within our MCT approach, the elastic constant appears discontinuously upon crossing the glass transition [i.e., $\lim_{\omega\to 0} G'(\omega)$ jumps from zero for $\epsilon\to 0^-$ to a finite value for $\epsilon\to 0^+$] thus demonstrating that the MCT indeed describes a transition to an amorphous solid.

3. Nonlinear stress response

By numerical solution of the equation of motion [Eq. (17)] we obtain the non-time-translational invariant density correlator $\Phi(t,t')$ and, via Eqs. (1) and (16), the nonlinear stress response. The numerical algorithm requires the equation of motion to be discretized over the entire two-dimensional (t,t') plane. While considerations of both causality $(t>t')$ and the periodicity of the correlator with respect to a translation in time $[\Phi(t+t_0,t'+t_0)=\Phi(t,t')$, where $t_0=\pi/\omega]$ enable certain simplifications to be made, calculation of the correlator over many decades in time remains a computationally demanding task.

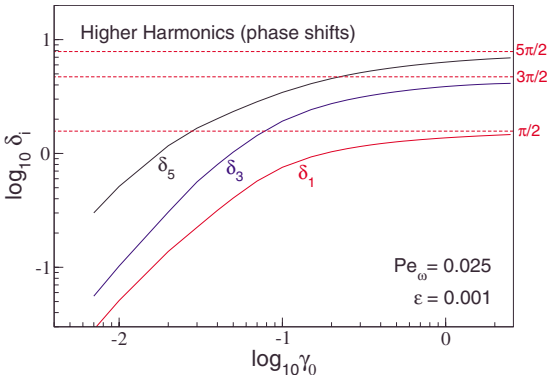

FIG. 7. (Color online) (Theory) The theoretical values for the first, third, and fifth phase shifts which contribute to the nonlinear stress response shown in Fig. 2. It should be noted that the phases are only physically meaningful, i.e., contribute significantly to the total $\sigma(t)$ signal when the corresponding intensities shown in Fig. 6 are non-negligible ($\epsilon=10^{-3}$ and $\mathrm{Pe}_\omega=0.025$).

Typical examples of the response $\sigma(t)$ for a glassy state ($\epsilon=0.001$) are shown in Fig. 3 for various values of the strain amplitude γ_0 at a fixed frequency. Alongside each of the time series we show the corresponding Lissajous curves indicating the extent of the dissipation [via the area enclosed, see Eq. (14)] and the deviations from nonlinearity (discernible from the nonellipticity of the loop). The value of ϵ employed to generate this figure generates a dynamic yield stress $\sigma_y=0.2763$, which is indicated in each panel of Fig. 3 by a broken red line. This can also be read-off from the appropriate flow curve in Fig. 1.

For small amplitudes $\gamma_0\leq 0.01$ the system is almost linear and responds in a predominately elastic fashion at the considered frequency. As γ_0 is increased, clear deviations from a sinusoidal response are apparent and higher harmonics start to contribute to the signal. In this nonlinear regime the stress response exhibits a characteristically flattened peak, with an asymmetry which increases as a function of γ_0. It is clear from the figure that the higher harmonics first become significant when the maximum value of the stress $\sigma(t)$ approaches the dynamic yield stress. An *idealized* yield stress material, subject to large amplitude oscillatory shear of vanishing frequency, would be expected to show a steady increase of the stress up to the yield point, beyond which the system begins to flow, maintaining $\sigma(t)=\sigma_y$ until the reversal of strain enables relaxation back to zero. If this was the case, then $\sigma(t)$ would be represented by a "clipped" signal, symmetric during loading and unloading of the sample.

The results presented in Fig. 3, however, have been generated for a low, but not vanishingly small, frequency. At finite frequency the maximum stress attainable in a system under steady shear is given by $\sigma_{\max}\equiv\sigma(\gamma_0\omega)$, where $\sigma(\dot{\gamma})$ is the stress on the steady shear flow curve. This maximal stress under flow, $\sigma_{\max}$, is indicated by a blue dotted line in Fig. 3 for the four largest strain amplitudes considered. In each case, once the stress exceeds the yield point the curve flattens, exhibiting a maximum which remains bounded from above by $\sigma_{\max}$. In the low-frequency limit the lower and upper bounds to the peak value of $\sigma(t)$ become equal, $\sigma_{\max}=\sigma_y$, such that the signal becomes clipped at the yield point. In order to test this hypothesis further, we show in Fig. 4 stress responses generated using the same parameter set as employed in Fig. 3, but for a frequency one order of magnitude lower. At this reduced frequency, the clipping of $\sigma(t)$ at yield is quite clear, although the peak stress still slightly exceeds σ_y due to the fact that the values of the strain-rate amplitude are not sufficiently small that $\sigma_{\max}$ has saturated to σ_y.

Two additional comments are in order regarding the results shown in Figs. 3 and 4. First, for low frequencies (e.g., the data shown in Fig. 4) the full time-dependent stress signal can be rather faithfully reproduced by a simple approximate expression. Defining $\sigma_1(t)\equiv\gamma_0[G_1'(\omega)\sin(\omega t)+G_1''(\omega)\cos(\omega t)]$ the stress is well approximated by

$$\sigma(t) = \begin{cases} \sigma_1(t), & \sigma_1 \leq \sigma_y \\ \sigma_y, & \sigma_1 > \sigma_y, \end{cases} \tag{26}$$

where G_1' and G_1'' are the lowest-order coefficients in Fourier series (10). In order to describe correctly the subyield response, $\sigma(t) \leq \sigma_y$, it is necessary to incorporate the γ_0 dependence of the lowest-order coefficients. It is also noteworthy that it is the dynamic, yield stress, which plays the crucial role in determining the time-dependent $\sigma(t)$. While the importance of dynamic yield in determining the oscillatory response is clear within the present approach, it remains to be seen whether this is a constraint introduced by employing a prescribed strain or, more significantly, an indication that the dynamic and static yield stresses are identical within our approximate theory. Simple approximation (26) contains higher harmonic contributions as a result of the yield stress clipping criterion.

4. Fourier analysis

In order to provide a more systematic analysis of the time signal $\sigma(t)$, we now consider its decomposition into the Fourier modes and investigate the behavior of the coefficients entering series (10) and (13) as a function of γ_0. We address first the strain amplitude dependence of G_1' and G_1'', thus mimicking the ubiquitous "strain sweep" experiments generally used to assess the nonlinear response of a given material. In Fig. 5 we show typical results for the lowest-order coefficients as a function of strain for two different values of the excitation frequency.

For small values of γ_0 linear response is recovered and the values of G_1' and G_1'' may be read-off from the data shown in Fig. 2. The linear-response regime persists up to around $\gamma_0=0.01$, beyond which G_1'' begins to increase gradually, reaching a maximum value at around $\gamma_0=0.1$. As noted in Sec. II C, the coefficient G_1'' is proportional to the amount of energy dissipated per oscillation cycle. The increase in dissipation observed over the range $\gamma_0=0.01 \rightarrow 0.1$ is probably connected to the increasing disruption of the microscopic "cage" structure of dense glassy systems, induced by the externally applied strain field. However, such microscopic interpretations remain purely speculative within the present context of schematic model calculations, for which there is no explicit spatial resolution of correlated density fluctuations.

Deeper insight into the microscopic mechanisms underlying the observed macroscopic response would be provided by solution of the full equations presented in [20]. The increase in G_1'' is associated with a decrease in G_1' as a function of γ_0. In contrast to G_1'', there exists no simple physical interpretation of the coefficient G_1' in the nonlinear regime. For strain amplitudes exceeding $\gamma_0=0.01$ the recoverable elastic energy becomes distributed over G_1' and the higher harmonics, such that G_1' loses its special status as a "storage modulus."

For $\gamma_0>0.1$ the dissipation G_1'' becomes larger than G_1', indicating a crossover from predominately elastic to predominately viscous response, and both functions exhibit a monotonic decay. For values of the strain amplitude larger than unity a regime of asymptotic decay is entered, characterized by a well-defined power-law dependence. We find that the numerically generated data are well fitted by power laws $G_1'' \sim \gamma_0^{-\nu}$ and $G_1' \sim \gamma_0^{-\nu'}$, with $\nu=0.65$ (± 0.02) and $\nu'=2\nu$. Moreover, calculations performed at various frequencies show that the exponent values are independent of ω and thus seem to represent a universal aspect of the asymptotic decay within the schematic model. While the numerical findings are suggestive of a universal exponent ν, analytical calculation of its precise value has so far proved elusive. The primary difficulty in extracting ν from the theory is that, even in the asymptotic regime, the correlator $\Phi(t,t')$ retains a residual dependence on the waiting time t' which does not yield readily to analytic treatment. The integral for stress (1) thus consists of a complicated superposition of correlators for different values of t'.

An important numerical prediction of the schematic model is that the exponents dictating the decay of G' and G'' are related, to within numerical accuracy, by a factor of 2. The relation $\nu'=2\nu$ has been observed in experimental studies of a variety of soft materials (see Sec. VI C for more details on this point) and it would therefore be of considerable interest to investigate this apparent prediction of our model in more depth. The relationship $\nu'=2\nu$ is found also in the simple nonlinear Maxwell models [26,43] and is thus not particularly surprising. Such models inevitably predict the trivial exponents $\nu=1$ and $\nu'=2$. The numerical data obtained by Miyazaki *et al.* [43] from solving their microscopic MCT theory are consistent with the exponent relation $\nu'=2\nu$ but predict a value of $\nu=0.9$ (obtained by fitting the numerical data), which differs somewhat from the experimental value $\nu=0.7$ for polymethyl methacrylate (PMMA) colloids presented in the same work. Whether the value $\nu=0.9$ from the MCT calculations in [43] is influenced by the additional isotropic approximations employed remains unclear.

The coefficients G_1' and G_1'' discussed above describe the response at the fundamental frequency. We now consider the contribution of the higher harmonic terms to the stress signal. Due to the $\dot{\gamma}(t)=-\dot{\gamma}(t)$ symmetry of $\sigma(t)$, even coefficients in Fourier series (13) are identically zero within the schematic theory (a condition which provides a useful check for our numerical algorithms). In Fig. 6 we show the intensities of the odd harmonics (normalized by I_1) up to $n=9$ for a glassy state, obtained by applying a discrete Fourier transform to the time series $\sigma(t)$. For very small amplitudes $\gamma_0<0.01$ the numerical solution of the equation of motion for $\Phi(t,t')$ becomes unreliable as the structural relaxation time exceeds the range of the numerical grid upon which the oscillating function $\Phi(t,t')$ can be resolved. Data are thus presented for $\gamma_0>0.01$ where accurate converged solutions can be obtained. At strain amplitude $\gamma_0=0.01$, only I_3 contributes significantly to the signal (around 3%). As the γ_0 is increased beyond 0.01, the increasing influence of I_3 is accompanied by the appearance of terms I_5, I_7 (beyond $\gamma_0=0.03$), and I_9 (beyond $\gamma_0=0.07$). Although intuitive, it is not clear *a priori* that the higher harmonics must necessarily appear in sequence $n=3,5,7,\ldots$ upon increasing the amplitude. All of the $I_{n>3}$ exhibit a maximum in the range $0.3<\gamma_0<1$ and by $\gamma_0=1$ contribute approximately half of the total signal,

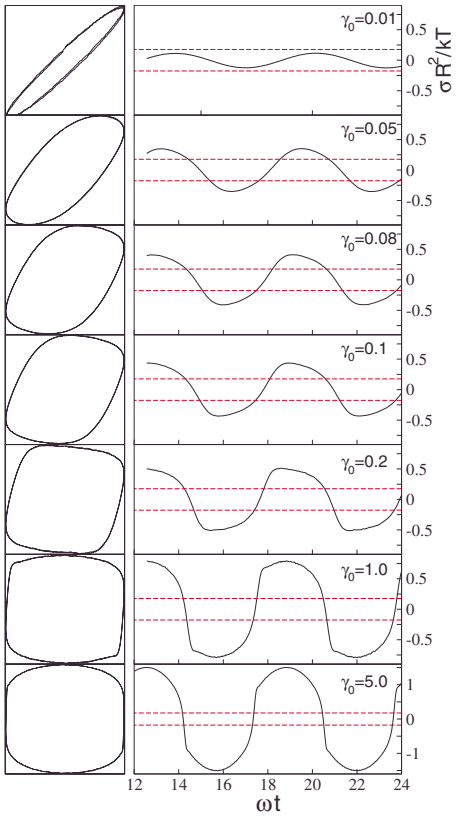

FIG. 8. (Color online) (Simulation) The stress response measured in the Brownian dynamics simulations of a binary hard-disk mixture under oscillatory flow. A size ratio of 1:1.4 was used to suppress crystallization. The considered strain amplitudes range from $\gamma_0=0.01$ to $\gamma_0=10$. The left column of figures shows the associated Lissajous curves illustrating the nonlinear character of the response. The simulations are performed at $\phi_{\mathrm{tot}}=0.81$ (slightly beyond the glass transition according to our simulation estimates). The Peclet number is $\mathrm{Pe}_\omega=0.05$).

$\Sigma_{n>1} I_n/I_1 \sim 0.5$. The maximum and subsequent decay of the higher harmonics has also been observed in [55].

Complementary to the higher harmonic intensities are the phase shifts δ_n shown in Fig. 7. It should be noted that the phases are only physically meaningful for amplitudes at which the corresponding intensity is significant. As γ_0 is increased toward unity the phases saturate to the asymptotic values $\delta_1=\pi/2$, $\delta_3=3\pi/2$, and $\delta_5=5\pi/2$. The higher harmonic contributions I_n and δ_n, which contribute for $\gamma_0>0.01$, describe the distortion of $\sigma(t)$ close to the yield stress (cf. Figs. 3 and 4).

B. Simulation results

In Fig. 8 we show the stress response measured in our Brownian dynamics simulations of a binary hard-disk mixture. As the strain amplitude is increased the simulated stress evolves from a linear to a nonlinear response for $\gamma_0>0.03$. Consistent with the theoretical results shown in Fig. 3, the time-dependent signal becomes distorted away from a pure sinusoid when the peak of $\sigma(t)$ encounters the dynamic yield stress. Although the Peclet number $\mathrm{Pe}_\omega=0.05$ is close to that employed in the theoretical calculations used to generate Fig. 3, the onset of the yield stress clipping effect, already manifest in Fig. 3, is not clear in the form of $\sigma(t)$ shown in Fig. 8. It would therefore seem likely that considerably smaller values of the Peclet number are required to observe this effect in our two-dimensional simulations. Nevertheless, the general form of the nonlinear stress is very similar on a qualitative level to that predicted by the schematic model in Fig. 3. Both simulation and theory exhibit a flattened and asymmetric peak which is skewed to the left.

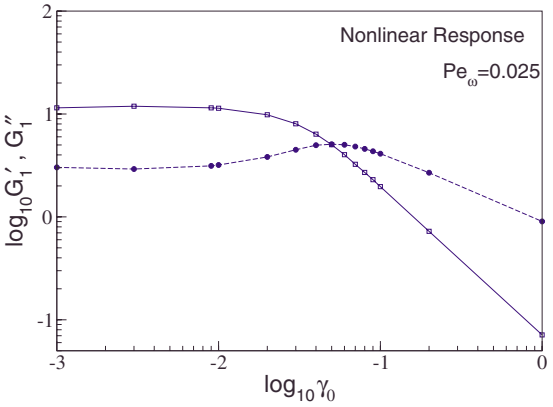

FIG. 9. (Color online) (Simulation) The simulation G_1' and G_1'' as a function of strain for two-dimensional volume fraction of 0.81 and Peclet number $\mathrm{Pe}_\omega=0.05$. For large values of γ_0 the moduli obey the power laws $G_1'' \sim \gamma_0^{-0.68}$ and $G_1' \sim \gamma_0^{-1.45}$.

In order to analyze more closely the stress signal we show in Figs. 9–11 the fundamental coefficients, higher harmonic intensities, and phase shifts, respectively. The dependence of G_n' and G_n'' on γ_0 is strongly reminiscent of that predicted by the schematic model (Fig. 5). Within the range $0.01<\gamma_0<0.06$ the system begins to deform plastically leading to a reduction in G_1' and an increase in G_1'' (and cross at $\gamma_0=0.05$), reflecting the increasing importance of dissipative processes. The height of the peak in G_1'' is rather less pronounced than that predicted by the schematic model. Beyond $\gamma_0=0.06$ both G_1' and G_1'' decrease monotonically, exhibiting an asymptotic power-law decay which is well described by the power laws $G_1'' \sim \gamma_0^{-0.68}$ and $G_1' \sim \gamma_0^{-1.45}$. Although these

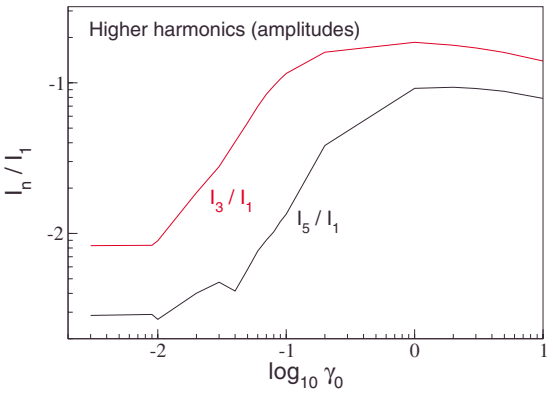

FIG. 10. (Color online) (Simulation) The normalized intensities of the third and fifth harmonics contributing to the nonlinear stress response shown in Fig. 8.

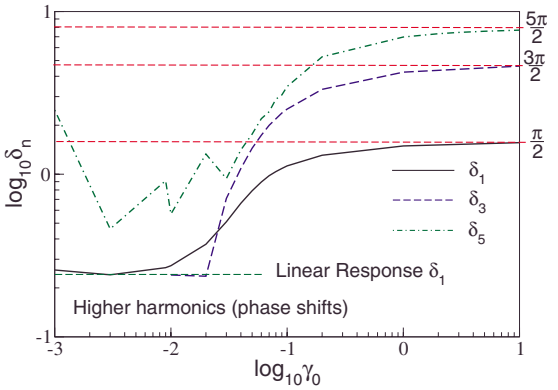

FIG. 11. (Color online) (Simulation) The phase shifts of the first and third harmonics contributing to the nonlinear stress response shown in Fig. 8.

values do not satisfy perfectly the empirical relation $\nu' = 2\nu$, the deviation of the simulation exponent ratio $\nu'/\nu = 2.13$ may well be attributable to numerical error. Despite this discrepancy, the absolute values of the exponents $\nu = 0.68$ and $\nu' = 1.45$ compare well with those emerging from the schematic model ($\nu = 0.65$ and $\nu' = 1.3$). The schematic model considered in the present work would thus seem to be more realistic than either a simple Maxwell model ($\nu = 1$ and $\nu' = 2$) or the microscopic MCT approach of Miyazaki *et al.* ($\nu = 0.9$ and $\nu' = 1.8$) at least on the basis of our simulation results.

In Fig. 10 we show the intensities of the third and fifth harmonics as a function of γ_0. Higher order terms were found to be highly susceptible to the effects of statistical noise in the simulation data and have thus been omitted. Upon increasing the strain amplitude beyond $\gamma_0 = 0.03$ the system leaves the linear-response regime and the contribution of the third harmonic grows. For strains exceeding around 0.1 the fifth harmonic also begins to play a significant role in determining the stress response. In keeping with the schematic model predictions, both I_3/I_1 and I_5/I_1 exhibit a maximum, albeit more sharply peaked and shifted to slightly larger strain values approaching unity. The corresponding phase shifts also share the general features of the schematic model predictions, in particular, for large values of γ_0 we find that δ_1, δ_3, and δ_5 saturate to $\pi/2$, $3\pi/2$, and $5\pi/2$, respectively. These results suggest that series (13) reduces to

$$\sigma(t) = \gamma_0 \sum_{n=1}^{\infty} I_{2n+1}(\omega)(-1)^n \cos[(2n+1)\omega t] \qquad (27)$$

for large values of γ_0.

C. Experimental results

1. Flow curves and linear-response moduli

In Fig. 12 we show the experimentally measured flow curves and in Fig. 13 the linear-response moduli for three different temperatures (corresponding to three different volume fractions). Reduced units are employed for both the control parameters,

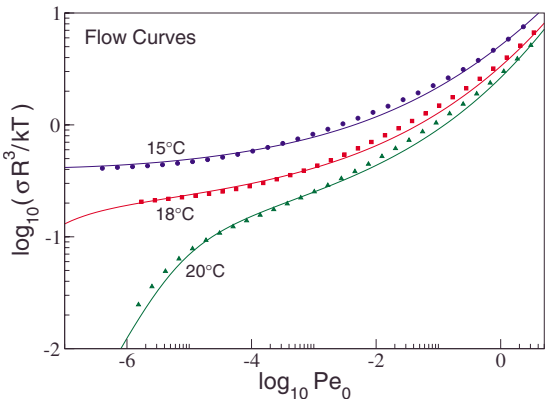

FIG. 12. (Color online) (Experiment) Symbols: the experimentally measured flow curves for three different temperatures, $T = 20.0\ ^\circ\mathrm{C}$ ($\phi_{\mathrm{eff}} = 0.57$), $T = 18.0\ ^\circ\mathrm{C}$ ($\phi_{\mathrm{eff}} = 0.60$), and $T = 15.0\ ^\circ\mathrm{C}$ ($\phi_{\mathrm{eff}} = 0.65$). Lines: theoretical fits to the data using the parameters in Table I.

$$\mathrm{Pe}_0 = \frac{\dot{\gamma} R_H^2}{D_0}, \quad \mathrm{Pe}_\omega = \frac{\omega R_H^2}{D_0}$$

(where D_0 is obtained from the solvent viscosity using Stokes' law), as well as for the shear stress and the moduli,

$$\sigma_{\mathrm{red}} = \frac{\sigma R_H^3}{k_B T}, \quad G'_{\mathrm{red}} = \frac{G' R_H^3}{k_B T}, \quad G''_{\mathrm{red}} = \frac{G'' R_H^3}{k_B T}.$$

For small Peclet numbers the flow curve measured at 20 °C (corresponding to $\phi_{\mathrm{eff}} = 0.57$) shows a first Newtonian plateau. As Pe_0 is increased we observe a decrease in viscosity, followed by a second Newtonian plateau, both of which are typical for a shear thinning fluid. The viscoelastic character of the sample at 20 °C is demonstrated by the linear-response moduli shown in Fig. 13. For intermediate frequencies G' and G'' cross, indicating the presence of a structural α-relaxation process.

The flow curve measured at the lower temperature 18 °C ($\phi_{\mathrm{eff}} = 0.60$) displays a more pronounced plateau region. However, for the lowest shear rates investigated a slight decrease from the plateau is evident, suggesting the existence of an α relaxation time which has shifted out of the experimental frequency window. The corresponding linear moduli shown in Fig. 13 show a plateau in G' characteristic of an arrested state (see, e.g., [56]). The plateau at intermediate values of Pe_ω is followed by a decrease for small Pe_ω values, consistent with the existence of a crossover point and, therefore, a fluid relaxation. This is especially apparent in $G''(\omega)$ which continues to rise as the frequency is decreased. Extrapolation of the measured data to lower frequencies suggests $\mathrm{Pe}_\omega^{\mathrm{cross}} \approx 10^{-6} - 10^{-7}$, where G' and G'' cross. For the lowest temperature investigated, 15 °C ($\phi_{\mathrm{eff}} = 0.65$), the flow curve exhibits a constant plateau down to the lowest values of Pe and the storage moduli remains constant at low Pe_ω. The sample at 15 °C may thus be considered as a glass for which additional "hopping" processes lead to an increase in G'' at low frequencies.

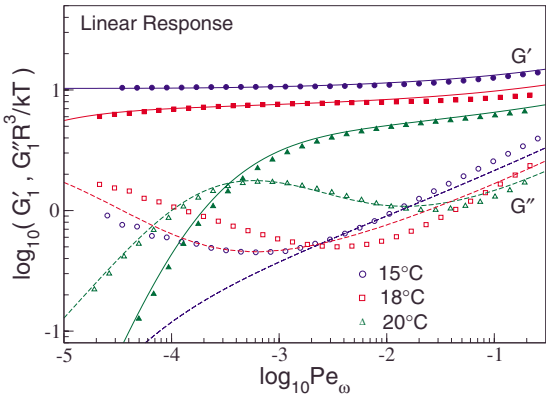

FIG. 13. (Color online) (Experiment) Symbols: the experimentally measured linear-response moduli for three different temperatures, $T=20.0$ °C ($\phi_{\text{eff}}=0.57$), $T=18.0$ °C ($\phi_{\text{eff}}=0.60$), and $T=15.0$ °C ($\phi_{\text{eff}}=0.65$). Lines: theoretical fits to the data using the parameters in Table I.

The procedure by which experimental data may be fit using the schematic $F_{12}^{\dot{\gamma}}$ model in [26] is already well documented [31]. Fitting the experimental data for the flow curve and linear moduli using the present schematic model proceeds analogously. For a given volume fraction, a fixed set of model parameters may be found which fit both the flow curve and the linear moduli. It is thus possible to determine the separation parameter ϵ, the vertex v_σ, and the decay rate Γ. The parameter γ_c is obtained as an additional parameter for the description of the flow curve. The high-frequency viscosity η_∞^ω is only important for the frequency spectrum (and is connected with the high shear viscosity $\eta_\infty^{\dot{\gamma}}$ via $\eta_\infty^{\dot{\gamma}}=\eta_\infty^\omega+v_\sigma/(2\Gamma)$ [30]). Fixing the parameters by these two experiments in the linear viscoelastic and the steady state determines all information needed to calculate the nonlinear oscillatory behavior (parameters are summarized in Table I). Therefore, the experimental data sets of the deformation sweeps (Figs. 14–16) and the oscillatory time tests (Figs. 17 and 18) are solely described by the theory of Sec. III and the fixed parameter sets obtained by fitting Figs. 12 and 13 without further modification. In this sense, the theoretical results to be presented for large amplitude oscillatory shear are predictions, as no further fitting is required.

2. Nonlinear response

The nonlinear regime has been tested using two different experiments: deformation sweeps at 1, 0.1, and 0.01 Hz (see Figs. 14–16) and oscillatory time series measured at 1, 0.1, and 0.01 Hz for various deformation amplitudes ranging from the linear to the nonlinear regime (see Figs. 17 and 18). The complete set of nonlinear oscillatory data is solely described by the schematic MCT employing the parameter sets determined by the fitting procedure described above.

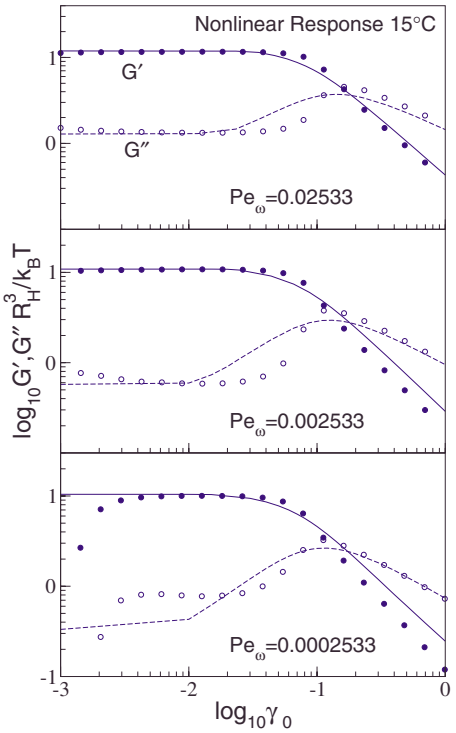

FIG. 14. (Color online) (Experiment) Strain sweeps at three different frequencies for the temperature 15.0 °C. Circles: experimental data. Lines: theoretical fits using the parameter set $(\epsilon, v_\sigma, \Gamma, \gamma_c, \tilde{x})$ obtained by simultaneously fitting the flow curves (Fig. 12) and linear-response moduli (Fig. 13).

In Fig. 14 we show the results of strain sweep experiments at 15 °C ($\phi_{\text{eff}}=0.65$) for three different values of Pe_ω. For strains up to around 1% the system shows linear-response behavior, beyond which dissipation starts to increase, leading to a growth of G'' up to a maximum in the range of 10–20 % strain. The growing dissipation and eventual crossing of G' and G'' as a function of γ_0 indicate the breaking of microscopic particle cages.

For higher deformations G' and G'' display a power-law decay. The exponents ν and ν' obtained at different temperatures and frequencies are given in Table II.

TABLE I. Schematic model parameters obtained by fitting experimental data for the flow curves (Fig. 12) and linear-response moduli (Fig. 13). These parameters are then used to make theoretical prediction for large strain amplitude oscillatory experiments.

T (°C)	ϕ_{eff}	ϵ	v_σ	Γ	γ_c	η_∞
20.0	0.57	-2.45×10^{-3}	59	100	0.18	42
18.0	0.60	-2.2×10^{-4}	85	100	0.19	36
15.0	0.65	5×10^{-5}	115	105	0.28	24

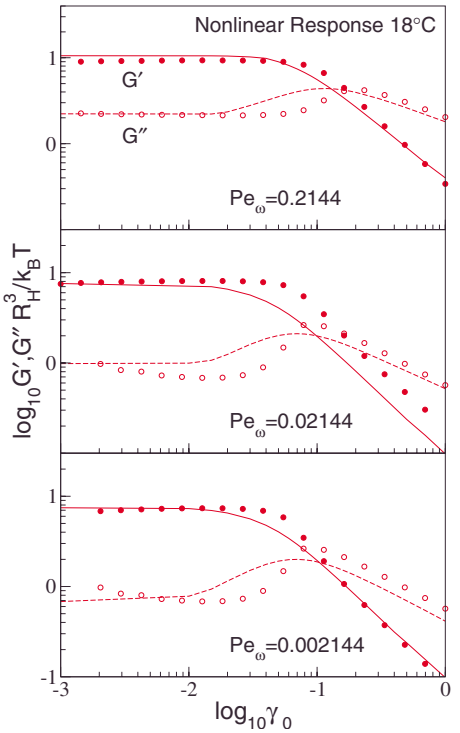

FIG. 15. (Color online) (Experiment) Strain sweeps at three different frequencies for the temperature 18.0 °C. Circles: experimental data. Lines: theoretical predictions.

The theoretical predictions shown in Fig. 14 are in good agreement with the experimental data and capture both the height and location of the maximum in G' rather well, although the departure from linear response appears to be less abrupt than in experiment, indicating a more gradual breaking of cages with increasing γ_0. We note that the discrepancy between theory and experiment in the linear-response regime for the lowest frequency considered has its origins in the linear moduli fits presented in Fig. 13. For glassy states there occur additional physical relaxation processes at low frequency which are manifest in an upturn of the linear response $G''(\omega)$ at low frequencies and which are not captured by mode-coupling based theoretical approaches. Particularly

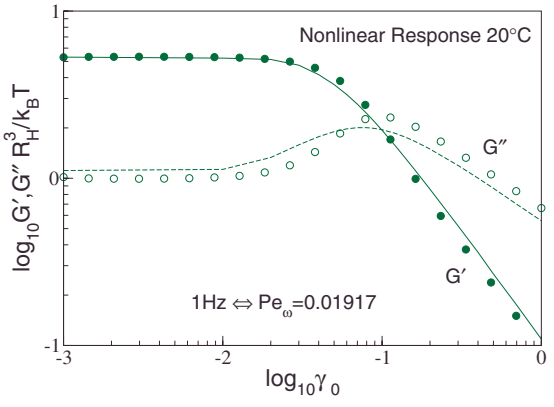

FIG. 16. (Color online) (Experiment) Strain sweeps at a fixed frequency Pe$_\omega$=0.019 17 for the temperature 20 °C. Circles: experimental data. Lines: theoretical predictions.

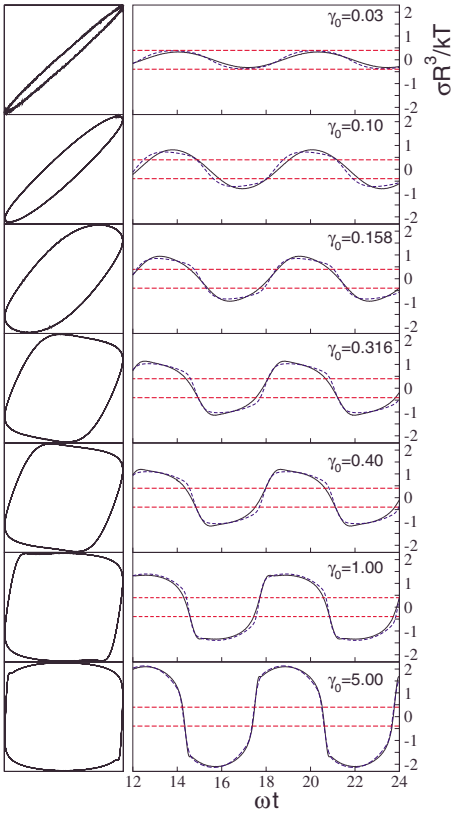

FIG. 17. (Color online) (Experiment) The stress response measured in LAOS experiments for strain amplitudes from γ_0=0.03 to γ_0=5 (black line) and the associated Lissajous figures illustrating the nonlinear character of the response. The experiments are performed at T=15.1 °C a glassy state and at a frequency of 1 Hz (corresponding to Pe$_\omega$=0.025 33). At γ_0=0.03 the response is almost entirely elastic, emphasizing the proximity of the quiescent state to the glass transition. At γ_0=5 the system is almost purely viscous. The increase in dissipation with increasing γ_0 is reflected in the increasing area enclosed by the closed Lissajous curves. The yield stress is indicated by the broken red lines. Theoretical results are given by broken blue lines.

significant is the agreement between theory and experiment in the large strain regime for which the cage structure has been broken up by the applied flow. The power-law decay of the experimental data is well described by the theoretical exponents ν=0.65 and ν'=1.3.

Both the numerically obtained theoretical results and experimental data shown here demonstrate the exponent relation $\nu' \approx 2\nu$ (as in the theory in [43]). It is interesting to note that although this relation does not appear to be truly universal, broadly similar behavior has been found for a variety of different materials, all of which show the deformation behavior classified by Hyun *et al.* [57] as type III (weak strain overshoot). A few examples are, e.g., a Xanthan gum solution [7] with $\nu'=-1.53$, $\nu=0.64$, and a ratio $\nu'/\nu=2.4$, anchor spreadable butter and promise spread which yield exponents $-2.1<\nu'<-2.0$ with $\nu=-0.9$ and a ratio of $\nu'/\nu=2.3$ or the hard-sphere solution of Miyazaki *et al.* [43] (PMMA spheres of 197 nm in a mixture of decaline and cycloheptylebromide) which show $\nu=0.7$ and $\nu'=1.4$.

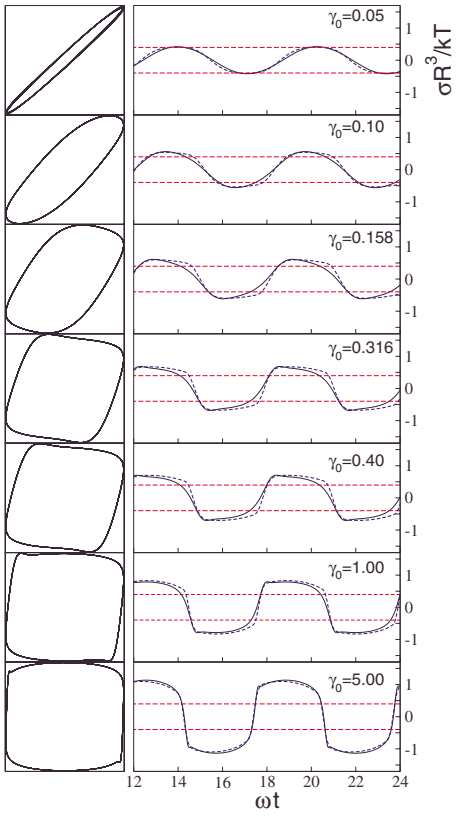

FIG. 18. (Color online) (Experiment) As in Fig. 17 but at a frequency of 0.1 Hz (corresponding to Pe_ω=0.002 533). Full black lines: experimental data. Broken blue lines: theoretical results. The yield stress is indicated by the broken red lines.

In Figs. 15 and 16 we show further strain sweep measurements for temperatures 18 °C (ϕ_{eff}=0.60) and 20 °C (ϕ_{eff}=0.57). The strain sweep measured at 20 °C is particularly well described by the theory and, taken together with the results shown in Figs. 12 and 13, demonstrates the accuracy with which the present schematic model may be used to describe the flow curve, linear moduli, and strain sweep data of a dense colloidal fluid using a single fixed set of model parameters.

For the oscillatory time series the schematic model calculations and the simulation are in good agreement with the experimental data. The direct comparison of theory and experiment for two frequencies (1 and 0.01 Hz), respectively, and the Peclet numbers (Pe_ω=0.025 and 0.0025) is given in Figs. 17 and 18. For small deformations, a linear viscoelastic behavior is indicated by the nearly perfect sinusoidal output signal but becomes distorted as the strain amplitude is increased. For Pe_ω=0.025 the stress signal displays flattened asymmetric peaks at intermediate values of γ_0, consistent with a regime of cage breaking around $\gamma_0=\gamma_c$. In contrast to the MCT predictions, the data show a pronounced dip at the top of the asymmetric peak. For high deformations, the peak shape approaches a semispherical shape with a vanishing but still visible dip or overshoot at the beginning edge of the peak. The stress wave form at intermediate amplitudes resembles qualitatively that observed in both wormlike micellar solutions [58] and entangled polymer solutions [59] when subject to large amplitude oscillation.

For the smaller frequency at Pe_ω=0.0025 indications of the effect of the merging σ_{max} and the yield stress are found. The peaks show in the intermediate and high deformation range a more cutoff shape, although the dip still remains, in contradiction to the MCT. The peak shape for middle γ_0 drops faster in the experiment as for the more boxlike shape of the MCT time signals. However, this shape is found in the experiment for high γ_0 as well. The fact that the stress measured at the lowest frequency (Fig. 18) appears to show a clipping above the dynamic yield stress may provide a signature of a static yield stress in the system. All together the experiments and the theory fit well for all compared Peclet numbers and amplitudes, although some small deviations of the shape exist. The predictive character of the schematic MCT model for the oscillatory time series is remarkable due to the fact that the shapes are not fitted but calculated with the parameter set defined from the flow curves and the frequency test in the linear viscoelastic regime.

3. Fourier analysis

In order to provide a more detailed analysis of the time series shown in Figs. 17 and 18 we have calculated the intensities and phase shifts [see Eq. (13)]. The phase shifts are calculated from the real and imaginary parts of the Fourier-transformed signal. Representative fast Fourier transform (FFT) spectra are shown in Fig. 19 for the measurements made at 15.1 °C, 1 Hz, and for amplitudes γ_0=0.03 and 1. The spectrum demonstrates that at this low strain amplitude

TABLE II. Experimentally measured values of the exponents ν and ν' dictating the decay of G' and G'' as a function of γ_0 for large values of γ_0.

T (°C)	ϕ_{eff}	f (Hz)	ν	ν'	ν'/ν
15.0	0.65	1	−0.63	−1.26	1.99
15.0	0.65	0.1	−0.74	−1.40	1.89
15.0	0.65	0.01	−0.79	−1.56	1.97
18.0	0.60	1	−0.63	−1.30	2.06
18.0	0.60	0.1	−0.71	−1.42	2.00
18.0	0.60	0.01	−0.82	−1.63	1.98
20.0	0.57	1	−0.63	−1.25	1.98

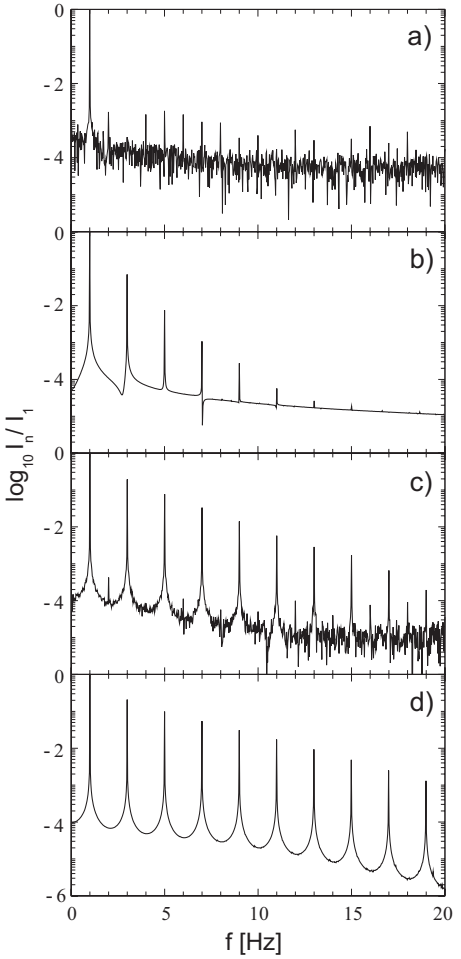

FIG. 19. (Experiment and theory) FFT spectra of the oscillatory time test signals. The experiment was performed at 15.1° and 1 Hz. (a) (experiment) and (b) (theory) are the FFT spectra at $\gamma_0=0.03$ and (c) (experiment) and (d) (theory) at an amplitude of $\gamma_0=1$.

the higher harmonics do not contribute significantly and have an intensity only around 0.1% of the basic harmonic I_1. Although peaks for even and odd harmonics are visible, their low intensities are not far away from the noise level. We therefore consider this measurement to be within the linear viscoelastic range.

At the same conditions the MCT calculations show a rather different picture [see Fig. 19(b)]. Although the time signals for this γ_0 do not deviate strongly from the experimental equivalent (see Fig. 17), the effect in the Fourier spectrum is noticeable (see Fig. 19). Up to the 11th harmonic all odd harmonics can be clearly separated from the baseline, with I_3/I_1 around 10%. Furthermore, in the theoretical FFT spectrum an exponential decay of the intensities is apparent, a feature which first becomes evident in the experimental data for $\gamma_0 \geq 0.158$. At the larger strain amplitude, $\gamma_0=1$, the MCT calculations and the experimental FFT spectra are very similar [see Figs. 19(c) and 19(d)]. The present theory thus provides a qualitative description of the higher harmonics which becomes quantitative as the strain amplitude becomes significant ($\gamma_0 \sim 1$). The theory provides a sensible interpolation between linear-response and large amplitude regimes, both of which are captured accurately.

Some insight into the origin of the discrepancies at small excitation amplitude may be obtained by considering the theoretical predictions for the buildup of stress following the onset of steady shear flow (see also [33]). Within the elastic regime (i.e., well below the "stress overshoot" identifying the yield strain) the system should display the Hookian behavior with a clearly defined elastic constant. However, schematic model calculations of the stress for this protocol (either using the present model or the $F_{12}^{\dot{\gamma}}$ model in [26]) exhibit deviations from the Hookian behavior at small strains. This feature of the schematic models is related to the slowness of the β decay of the transient density correlator onto the plateau. We can thus speculate that the discrepancy between the Fourier spectra of theory and experiment at low values of γ_0 may be due to the excessively slow decay of the correlator to its plateau value, which is an inherent feature of any model based on the original schematic F_{12} model [25,39,40].

In Fig. 20(a) the amplitude dependence of the experimentally measured third harmonic is shown for three different frequencies in the glass (15.1 °C). It can be seen that as the frequency is reduced, the onset of the nonlinear regime, indicated by increase of the normalized third harmonic intensity, moves to lower values of γ_0. In Fig. 20(b) we show the same quantity at a fixed frequency of 1 Hz for three different temperatures. Surprisingly no strong influence of a change in the volume fraction is found, apart from a small deviation in the onset of the nonlinear regime in the glassy state, which is shifted to higher deformations. The only significant deviation for the volume fractions considered occurs at intermediate deformations, as the starting and end values coincide.

The phase shifts are given for the measurement at 1 Hz ($\mathrm{Pe}_\omega=0.025$) and 15 °C in Fig. 20(c). In the case of the fundamental δ_1 the phase shift is found as expected to start at 0° for small amplitudes and to end at 90° for high deformations, which corresponds to a cosine. The curve progression of the experimental data and the MCT calculation fits perfectly for δ_1. The theory deviates for the phase shifts of the higher harmonics due to the excessive contribution of nonlinearities at lower γ_0. However, the limiting values for high deformations are found to coincide ($\frac{\pi}{2}$ for δ_1, $\frac{3\pi}{2}$ for δ_3, and $\frac{5\pi}{2}$ for δ_5).

We have also included the data from our two-dimensional simulations into Figs. 20(c) and 20(d). In order to obtain a reasonable comparison we found it necessary to empirically multiply the strain employed in the simulations be a factor of 3, $\gamma_0=3\gamma_0^{sim}$. That such an empirical rescaling is necessary is not surprising given that only qualitative comparison is to be expected when comparing three-dimensional experimental results with those of two-dimensional simulations. It is therefore gratifying that the phases of the rescaled γ_0^{sim} are found to describe the experimental data very well, not only for δ_1 but also for δ_3 and δ_5.

The experimentally measured I_3/I_1 at 15.1 °C and 1 Hz is found to indicate the onset of the transition from linear to nonlinear regime at around $\gamma_0=0.04-0.05$. This can be seen by comparing with the strain sweep data. It shows the maximum of G'' at $\gamma_0 \approx 0.16$, which is connected with the breaking of the cages. This value could be correlated with the raising of I_5/I_1 above the "noise" level of $0.1\% \cdot I_n/I_1$. The

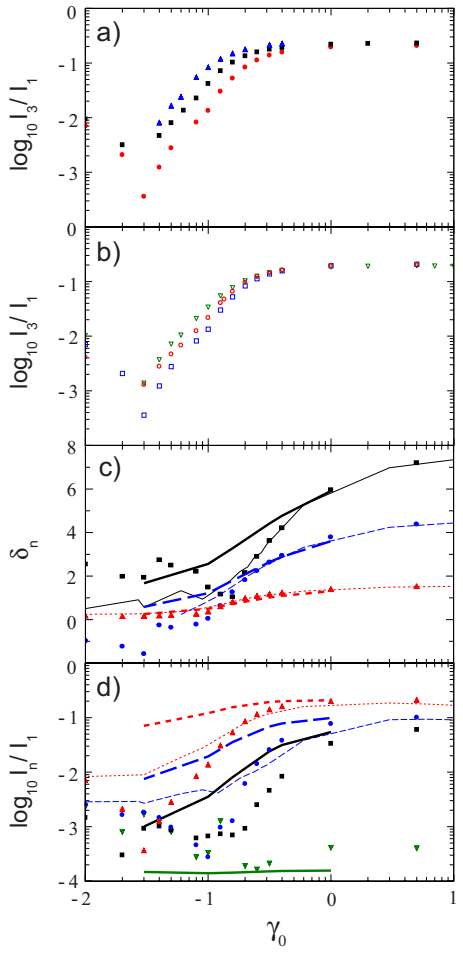

FIG. 20. (Color online) (Experiment, simulation, and theory) (a) I_3/I_1 at 15.1 °C for different frequencies (red circle: 1 Hz; black square: 0.1 Hz; and blue triangles up: 0.01 Hz). (b) Temperature dependence of I_3/I_1 at 1 Hz: 15.1 °C (blue squares), 18.4 °C (red circles), and 20.9 °C (green triangles down). (c) Experimental phase shifts (symbols) for 15.1 °C at 1 Hz. The simulation data are plotted versus $\gamma_0=3\gamma_0^{sim}$ as thin lines. The MCT calculations are given in thick lines. The phase shifts are δ_1 (red triangles up and dotted lines), δ_3 (blue circles and dashed lines), and δ_5 (black squares and solid lines). (d) Normalized intensities at 15.1 °C and 1 Hz; symbols mark the experimental data, thick lines the FFT of the MCT time signals, and thin lines the shifted simulation results: I_2/I_1 (green triangles down and solid line), I_3/I_1 (red triangles up and dotted lines), I_5/I_1 (blue circles and dashed lines), and I_7/I_1 (black squares and solid line).

description of I_3/I_1 is possible with the formula obtained by Wilhelm ($I_{3/1}(\gamma_0)=A\{1-[1+(B\gamma_0)^c]^{-1}\}$) [5]. For all experimental data the exponent c or the slope of the increase is found to be in the range of 2.2–2.7. The rescaled simulation results for the harmonics describe the experiment rather closely, whereas the MCT calculations are found to show a different behavior. All odd harmonics start at low γ_0 at higher values, whereas for high deformations the intensities coincide with the experimental results. Thus, also the slope of I_3/I_1 in this diagram changed to $c\approx 1.7$ instead of the experimental $c=2.7$. These discrepancies between experiment and theory may well be attributable to the slow decay of the correlator to the plateau, as discussed above.

Whereas the mode-coupling calculations show a very early transition from the linear to the nonlinear regime at $\gamma \approx 0.01$ (see Figs. 14–16), for reasons discussed above, the experiments for the frequencies and temperatures investigated show a deviation from linear behavior at $\gamma \approx 0.04-0.05$. For the rescaled simulation results of Fig. 9, the deviation starts at $\gamma\approx 0.03$. The onset of the yielding process is correlated with the onset of higher harmonics, starting with the third harmonic [see Fig. 20(d)]. Although the difference of the onset and intensity of the higher harmonics between theory and experiment is significant, the time signals are only slightly influenced (Figs. 17 and 18). The FFT is a very sensitive method to analyze the time signals, so very small deviations in the time signal can cause a remarkable difference in the spectra. Increasing the strain amplitude results in more asymmetric time signals with maxima and minima shifted to the left.

It was found in experimental, theoretical, and simulation strain sweeps that the maximum of G_1'' lies very close to the crossing point of $G_1'(\gamma_0)$ and $G_1''(\gamma_0)$. For the glassy sample ($\phi=0.65$) this point was located at $\gamma\approx 0.15$. Beyond this value, the fifth harmonic begins to increase, which can be seen in Fig. 20(d) for the experimental and rescaled simulation data. The theoretical time signals do not show such a sharp transition from the linear to the nonlinear regime. Furthermore, the simulation data start at higher intensity ratios as the experiment, an effect even more pronounced for the theoretical data. The schematic model thus predicts a more gradual transition between solid and fluid. The onset of the fifth harmonic was also found for micrometer sized particles [60] to be correlated with the crossing point of G_1' and G_1''. The view that the yield strain is indicated by the onset of the fifth harmonic is supported by the results of Le Grand and Petekidis [61]. For larger deformations, the time signals show a strain softening behavior, which is typical for shear thinning fluids. The phase shifts of experiment, simulation, and theory approach the limiting values of $n\cdot\pi/2$, where n is the index of the harmonic. In addition, the harmonics for theory and experiment show the same limiting values at large γ_0 for each harmonic (21% for I_3/I_1, 10% for I_5/I_1, 6% for I_7/I_1, and 4% for I_9/I_1). Furthermore, the theoretical harmonics exhibit a slight decrease at the highest calculated strains, which is not observed in the experimental data perhaps due the choice of a too small measurement range. In the simulation the decrease of the intensities is much more pronounced for high deformations, as the intensities do not show a plateau but only a maximum (at 18% for I_3/I_1 and at 8% for I_5/I_1).

VII. CONCLUSION AND OUTLOOK

We have used a combination of theory, experiment, and simulation to investigate the nonlinear stress response of dense colloidal dispersions under large amplitude oscillatory shear flow. The theory employed is a recent extension [23] of the well-studied $F_{12}^{\dot{\gamma}}$ model [26]. A key physical mechanism captured by the theory is the yielding of local particle cages and the subsequent onset of nonlinearity. In contrast to a

related approach presented by Miyazaki *et al.* [41,43], the theory employed here makes predictions for the higher harmonic contributions to the stress signal and thus enables the extent of the linear-response regime to be addressed. In order to make contact with experiment, the theory requires only the simultaneously determined parameters from the steady-state flow curve and the frequency dependence of the linear moduli to make predictions for the nonlinear viscoelastic response. We have thus compared the theory with rheological experiments performed on concentrated suspensions of thermosensitive core-shell particles.

The first nonlinear experiment considered was a strain sweep, performed at three different volume fractions and frequencies. Here we found very good agreement between experiment and theory, although there are small deviations concerning the onset of the nonlinear viscoelastic regime. The values of G_1' and G_1'' in the linear regime, the crossing point of G_1' and G_1'', maximum of G_1'', and asymptotic large strain behavior of G_1' and G_1'' are all well described by the theory. The Brownian simulation of a two-dimensional system of hard disks enables only a qualitative comparison but shows behavior broadly consistent with our experimental data, indicating that the yielding process is not strongly dependent on either the material details or dimensionality of the sample. Moreover, the simulations do not contain hydrodynamic interactions, suggesting that these are not of great importance for yielding. The ratio of the slopes of G_1' and G_1'' for large γ_0 in the shear molten state yields the exponent ratio $\nu'/\nu = 2.0 \pm 0.1$ in theory simulation and experiment. The fact that various other materials (of type III in [57]) display similar asymptotic behavior may suggest a universal mechanism underlying the oscillatory response of shear molten viscoelastic fluids.

The second type of experiment considered was oscillatory time sweeps. In this case the cage yielding is expressed by the deviation of the signal from a sinusoidal form, showing a characteristic asymmetric peak in the yielding regime, which is followed in the shear molten state by a typical strain softening semicircular peak shape. The agreement of the time signals obtained from theory, simulation, and experiments is good. However, small deviations in the time series obtained using the three methods lead to stronger deviations in the parameters of the Fourier-transformed time signals. This serves to emphasize the fact that FT rheology is a very sensitive method, sensitive on the logarithmic scale, capable of detecting, e.g., the fifth harmonic, to an accuracy of less than 1 promille. This analysis has shown that the onset of the third harmonic heralds the start of the nonlinear regime and that the maximum in G_1'', which here approximately coincides with both crossing points of G_1' and G_1'', and the yield strain are correlated with the onset of the fifth harmonic. Moreover, the plateau values of the phase shifts at high deformations are found to follow $n \cdot \pi/2$, with n being the index of each harmonic.

Despite the good overall level of agreement between theory and experiment there remain aspects which could be improved. First, the extent (in γ_0) of the linear-response regime is apparently too small within the present theory, with consequences for the variation of the higher harmonic intensities with amplitude. As noted, this failing has its origins in the quiescent transient density correlators predicted by the F_{12} model, upon which our more recent schematic model is based. It would thus be desirable to improve this fundamental aspect of the theory. Second, the stress response measured in experiment displays a more asymmetric wave form than that predicted by the schematic model. This aspect can potentially be connected to the fact that our model, when applied to calculate the buildup of stress upon the onset of shear, does not generate a stress overshoot. While a stress overshoot does occur in approximate solutions of the fully microscopic mode-coupling expressions [33], this aspect is lost in making ansatz (16) for the shear modulus as the strain dependent vertex functions appearing in the microscopic theory are replaced by a constant v_σ. Empirically, reincorporating a strain dependence into the theory via the replacement $v_\sigma \rightarrow v_\sigma(\gamma_0)$, such that the overshoot is recovered, may also lead to an increased wave-form asymmetry in the stress response and, thus, better agreement with experiment. However, when modifying the schematic model in this fashion, care must be taken not to destroy its existing positive features.

To summarize, it can be concluded that the schematic mode-coupling model [23] can make accurate predictions in the nonlinear viscoelastic regime based purely on parameters fixed by the steady-state stress and linear viscoelastic behavior. This constitutes the first truly time-dependent test (other than step strain) of the schematic model proposed in [23]. The Fourier transform analysis of time series obtained for various strain amplitudes and frequencies provides a wealth of experimental information regarding the mechanical response of a material. As our present experimental setup enables the investigation of transient flows, we anticipate that the study of such flow protocols, in combination with the present results, should enable a complete rheological characterization of our colloidal system.

ACKNOWLEDGMENTS

Thanks to M. Schwall, J. Grzanna, and A. Salah for helping with the programming of the FT program. Financial support was provided by the SFB TR6, Swiss National Science Foundation (J.M.B.), and the SFB 481 (M.S.).

[1] R. G. Larson, *The Structure and Rheology of Complex Fluids* (Oxford University Press, Oxford, 1998).
[2] P. Coussot, *Rheometry of Pastes, Suspensions, and Granular Materials* (Wiley, New York, 2005).
[3] R. G. Larson, *Constitutive Equations for Polymer Melts and Solutions* (Butterworths, London, 1988).
[4] M. Wilhelm, D. Maring, and H.-W. Spiess, Rheol. Acta **37**, 399 (1998).
[5] M. Wilhelm, Macromol. Mater. Eng. **287**, 83 (2002).
[6] R. H. Ewoldt, C. Clasen, A. E. Hosoi, and G. H. McKinley, Soft Matter **3**, 634 (2007).
[7] R. H. Ewoldt, P. Winter, J. Maxey, and G. H. McKinley, Rheol. Acta **49**, 191 (2010).
[8] R. H. Ewoldt, A. E. Hosoi, and G. H. McKinley, J. Rheol. **52**, 1427 (2008).
[9] F. Rouyer, S. Cohen-Addad, R. Höhler, P. Sollich, and S. M. Fielding, Eur. Phys. J. E **27**, 309 (2008).
[10] C. O. Klein, H.-W. Spiess, A. Calin, C. Balan, and M. Wilhelm, Macromolecules **40**, 4250 (2007).
[11] M. Wilhelm, P. Reinheimer, and M. Ortseifer, Rheol. Acta **38**, 349 (1999).
[12] S. A. Rogers and D. Vlassopoulos, J. Rheol. **54**, 859 (2010).
[13] K. A. Cho, K. Hyun, K. H. Ahn, and S. J. Lee, J. Rheol. **49**, 747 (2005).
[14] R. B. Bird, R. C. Armstrong, and O. Hassager, *Dynamics of Polymeric Liquids* (Wiley, New York, 1987).
[15] C. Truesdell and W. Noll, *The Nonlinear Field Theories of Mechanics* (Springer, Berlin, 1965).
[16] P. Sollich, F. Lequeux, P. Hebraud, and M. E. Cates, Phys. Rev. Lett. **78**, 2020 (1997).
[17] S. M. Fielding, P. Sollich, and M. E. Cates, J. Rheol. **44**, 323 (2000).
[18] C. Derec, G. Ducouret, A. Ajdari, and F. Lequeux, Phys. Rev. E **67**, 061403 (2003).
[19] J. M. Brader, Th. Voigtmann, M. E. Cates, and M. Fuchs, Phys. Rev. Lett. **98**, 058301 (2007).
[20] J. M. Brader, M. E. Cates, and M. Fuchs, Phys. Rev. Lett. **101**, 138301 (2008); see also the associated Viewpoint article in Physics **1**, 22 (2008).
[21] M. Fuchs and M. E. Cates, Phys. Rev. Lett. **89**, 248304 (2002).
[22] M. Fuchs and M. E. Cates, J. Rheol. **53**, 957 (2009).
[23] J. M. Brader, Th. Voigtmann, M. Fuchs, R. G. Larson, and M. E. Cates, Proc. Natl. Acad. Sci. U.S.A. **106**, 15186 (2009).
[24] J. M. Brader, J. Phys.: Condens. Matter **22**, 363101 (2010).
[25] W. Götze, in *Liquids, Freezing and Glass Transition*, edited by J.-P. Hansen, D. Levesque, and J. Zinn-Justin (North-Holland, Amsterdam, 1991), p. 287.
[26] M. Fuchs and M. E. Cates, Faraday Discuss. **123**, 267 (2003).
[27] D. Hajnal and M. Fuchs, Eur. Phys. J. E **28**, 125 (2009).
[28] M. Fuchs and M. Ballauff, J. Chem. Phys. **122**, 094707 (2005).
[29] J. J. Crassous *et al.*, J. Chem. Phys. **125**, 204906 (2006).
[30] J. J. Crassous, M. Siebenbürger, M. Ballauf, M. Drechsler, D. Hajnal, O. Henrich, and M. Fuchs, J. Chem. Phys. **128**, 204902 (2008).
[31] M. Siebenbürger, M. Fuchs, H. Winter, and M. Ballauff, J. Rheol. **53**, 707 (2009).
[32] V. Carrier and G. Petekidis, J. Rheol. **53**, 245 (2009).
[33] J. Zausch, J. Horbach, M. Laurati, S. U. Egelhaaf, J. M. Brader, T. Voigtmann, and M. Fuchs, J. Phys.: Condens. Matter **20**, 404210 (2008).
[34] J. K. G. Dhont, *An Introduction to the Dynamics of Colloids* (Elsevier, Amsterdam, 1996).
[35] N. G. van Kampen, *Stochastic Processes in Physics and Chemistry* (North-Holland, Amsterdam, 1981), Chap. XV.
[36] See any standard text on Fourier series, e.g., M. L. Boas, *Mathematical Methods in the Physical Sciences* (Wiley, New York, 1983).
[37] K. Hyun and M. Wilhelm, Macromolecules **42**, 411 (2009).
[38] J. A. Lissajous, Ann. Chim. Phys. **51**, 147 (1857).
[39] W. Götze, Z. Phys. B: Condens. Matter **56**, 139 (1984).
[40] W. Gotze and L. Sjögren, Rep. Prog. Phys. **55**, 241 (1992).
[41] K. Miyazaki and D. R. Reichman, Phys. Rev. E **66**, 050501(R) (2002).
[42] K. Miyazaki, D. R. Reichman, and R. Yamamoto, Phys. Rev. E **70**, 011501 (2004).
[43] K. Miyazaki, H. M. Wyss, D. A. Weitz, and D. R. Reichmann, Europhys. Lett. **75**, 915 (2006).
[44] H. M. Wyss, K. Miyazaki, J. Mattsson, Z. Hu, D. R. Reichman, and D. A. Weitz, Phys. Rev. Lett. **98**, 238303 (2007).
[45] M. Bayer, J. M. Brader, F. Ebert, M. Fuchs, E. Lange, G. Maret, R. Schilling, M. Sperl, and J. P. Wittmer, Phys. Rev. E **76**, 011508 (2007).
[46] A. Scala, Th. Voigtmann, and C. De Michele, J. Chem. Phys. **126**, 134109 (2007).
[47] O. Henrich, F. Weysser, M. E. Cates, and M. Fuchs, Philos. Trans. R. Soc. London, Ser. A **367**, 5033 (2009).
[48] W. Schaertl and H. Sillescu, J. Stat. Phys. **77**, 1007 (1994).
[49] R. N. Bracewell, *The Fourier Transform and Its Application*, 2nd ed. (McGraw-Hill, New York, 1986).
[50] C. Klein, Ph.D. thesis, Johannes-Gutenberg-Universität, 2005.
[51] T. Neidhöfer, Ph.D. thesis, Johannes-Gutenberg-Universität, 2003.
[52] K. Schmidt-Rohr and H. W. Spiess, *Multidimensional Solid State NMR and Polymers* (Academic Press, New York, 1994).
[53] D. van Dusschoten and M. Wilhelm, Rheol. Acta **40**, 395 (2001).
[54] D. A. Skoog and J. J. Leary, *Principle of Instrumental Analysis*, 4th ed. (Harcourt Brace College Publishers, Orlando, 1992).
[55] S. Kallus, N. Willenbacher, S. Kirsch, D. Distler, T. Neidhöfer, M. Wilhelm, and H. W. Spiess, Rheol. Acta **40**, 552 (2001).
[56] M. Laurati *et al.*, J. Chem. Phys. **130**, 134907 (2009).
[57] K. Hyun, S. H. Kim, K. H. Ahn, and S. J. Lee, J. Non-Newtonian Fluid Mech. **107**, 51 (2002).
[58] P. E. Boukany and S. Q. Wang, Macromolecules **41**, 1455 (2008).
[59] J. G. Nam, K. H. Ahn, and S. J. Lee, J. Rheol. **54**, 1243 (2010).
[60] L. Heymann, S. Peukert, and N. Aksel, J. Rheol. **46**, 93 (2002).
[61] A. Le Grand and G. Petekidis, Rheol. Acta **47**, 579 (2008).